A spinning disc study of fouling of cold heat transfer surfaces by gel formation from model food fat solutions

Jen-Yi Huang, Y.M. John Chew and D. Ian Wilson*
Department of Chemical Engineering and Biotechnology, University of Cambridge, New Museums Site, Pembroke Street, Cambridge, CB2 3RA, UK
Department of Chemical Engineering, University of Bath, Claverton Down, Bath, BA2 7AY, UK

Corresponding author
Dr D. Ian Wilson
Department of Chemical Engineering and Biotechnology
University of Cambridge
New Museums Site
Pembroke Street
Cambridge
CB2 3RA, UK

E-mail diw11@cam.ac.uk
Tel +44 1223 334791
FAX +44 1223 334976

A spinning disc study of fouling of cold heat transfer surfaces by gel formation from model food fat solutions

Huang, J.Y., Chew, Y.M.J. and Wilson, D.I.
Department of Chemical Engineering and Biotechnology, University of Cambridge, New Museums Site, Pembroke Street, Cambridge, CB2 3RA, UK
Department of Chemical Engineering, University of Bath, Claverton Down, Bath, BA2 7AY, UK

Abstract

The formation of immobile gels on heat transfer surfaces (‘coring’) caused by cooling fat solutions below their cloud point was studied using a novel spinning disc apparatus (SDA). The SDA features a cooled, removable heat transfer surface with well defined heat and mass transfer characteristics. Measurements of heat flux were combined with computational fluid dynamics simulations to yield reliable estimates of the surface temperature and shear stress. Fouling studies were performed with model solutions of 5 wt% tripalmitin in a paraffin oil operating in the ‘cold start’ mode, wherein the experiment starts with the surface colder than the steady state, simulating one mode of operating a standard ‘cold finger’ experiment. Local heat flux measurements allowed the thermal fouling resistance to be monitored: deposit mass coverage and composition were also measured. The cold surface promotes the rapid formation of an initial gel layer, followed by a period of linear fouling, and finally falling rate fouling behaviour. The linear fouling rate was relatively insensitive to temperature and shear rate, while the fouling rate in the falling rate regime was found to depend on the temperature driving force for crystallisation kinetics. The solids fraction within the deposit layer increased over the duration of a 12 h fouling test, indicating rapid ageing. The rheological properties of the deposits were highly sensitive to solids fraction.

Keywords: crystallisation, fats, fouling, freezing, gel

1. Introduction

The accumulation of unwanted solids on process surfaces is a persistent problem. These materials usually have low thermal conductivity, creating significant resistance to heat transfer. This fouling deposition can also cause partial or complete blockage of piping and process equipment, reducing flow rate together with increasing pressure drop. The formation of deposits from liquid fats on cold surfaces can affect both heat exchangers and distribution lines in the food sector. This 'coring' of distribution lines can impair product quality by contamination and by harbouring micro-organisms, as well as reducing the performance of trace heating or cooling designed to maintain the fat in a particular state.

Coring is an example of crystallisation fouling, which Epstein (1983) defined as deposition resulting from solubility differences, such that solids are generated from solution at the heat transfer surface. The fouling layer can form via heterogeneous growth on the surface, as in water scaling, or by crystallisation of the higher melting point components in the solution at the cold interface to yield a viscous, immobile gel which can harden to give a semi-solid deposit over time. The formation of a viscous gel layer is studied here using model solutions of a high melting point fat, tripalmitin (PPP), in a non-solidifying paraffin solvent.

Food fats are multi-component mixtures and coring shares many features with wax deposition in subsea crude oil pipelines (Elphingstone *et al.*, 1999; Ribeiro *et al.*, 1997). The major components are triglycerides, with smaller quantities of diglycerides, and these crystallise when the temperature falls below their cloud point, T_c. The cloud point is defined as the temperature at which the solid particles are first detected, and is lower than the equilibrium melting temperature for a given composition, as cooling-driven crystallisation requires the solution to be supersaturated. Nucleation is a kinetic process, however, and a crystal seed or foreign surface can promote heterogeneous nucleation and growth in this region (Mullin, 1993). The general scenario for crystallisation fouling of food fats is that the solution must firstly reach supersaturation, followed by nucleation and orientation of crystallites, ending up with aggregation and growth of the crystals (Hartel, 2001; Walstra *et al.*, 2001). Whereas a number of models have been reported for deposition on oil pipelines from waxy crudes (Akbarzadeh and Zougari, 2008; Bidmus and Mehrotra, 2004; Singh *et al.*, 2000) freezing fouling in food fats has attracted relatively little attention:

Fernandez-Torres *et al.* (2001) presented a fouling regime map of binary fat/solvent solutions based on simple thermodynamic and heat transfer relationships, and developed a heat transfer based model for coring in pipes carrying a laminar flow of fat. The controlling step in deposit growth is largely unknown, and key mechanisms, whether normal growth (Jackson and Chalmers, 1956), two-dimensional nucleation (Hillig, 1966) or screw dislocation (Hillig and Turnbull, 1956), remain to be identified.

Freezing fouling may occur at rest, such as in a reservoir, or under conditions of high shear rate and large temperature gradients, as in a scraped surface heat exchanger. For this reason, several experimental studies have investigated the effect of thermo-mechanical history on fouling behaviour. The temperature difference between the bulk liquid and the cold wall is generally regarded as the thermal driving force for deposition. Bidmus and Mehrotra (2004) reported an increase in wax deposition from oils with an increase in the temperature difference across the deposit layer. Increasing the flow rate may cause deposit removal because of the higher shear force. Other studies (Singh *et al.*, 2000) have shown that under conditions of constant temperature difference between the bulk crude oil and deposit/oil interface, the deposit thickness decreased as the Reynolds number was increased under both laminar and turbulent flow conditions. Most tests employ constant overall temperature difference: as deposit accumulates, the solution-deposit interface temperature rises and the driving force for deposition decreases. Fouling resistance-time (R_f - t) plots usually exhibit falling rate or asymptotic fouling behaviour (Epstein, 1983) and can often be fitted to the Kern-Seaton (1959) model, even though this model attributes the observed retardation to increased 'removal' as the deposit grows rather than temperature effects. Deposit removal by mechanisms such as spalling can occur, as reported by Fitzgerald *et al.* (2004).

The most commonly used experimental configurations for studying freezing fouling in waxy crude oils are the flow cell loop (Fitzgerald *et al.*, 2004; Parthasarathi and Mehrotra, 2005) and the coldfinger (Jennings and Weispfennig, 2005). Recently, Nigo *et al.* (2009) reported the design and operation of a novel spinning disc apparatus (SDA) featuring a cooled, rotating, vertical cylinder where deposition occurs on the cold, removable base (the sides are insulated). Food fat fouling behaviour is investigated here using a modified version of the SDA reported by Nigo *et al.* The SDA was fitted with a heat flux sensor which allows the change in local thermal fouling resistance, R_f, to be monitored. Model solutions of 5 wt% PPP in a paraffin oil, similar to those used by Fitzgerald *et al.* (2004) and Nigo *et al.* (2009),

were studied and the effects of disc rotation speed, ω_d, time, and temperature driving force on fouling behaviour were investigated. The thermal performance of the SDA was characterised more fully using computational fluid dynamics (CFD) simulations, so that surface temperature and surface shear stress could be predicted and manipulated readily. The deposit gels formed were analysed to track changes in composition resulting from ageing as reported for wax deposits by Singh *et al*. (2001b).

2. Materials and methods

2.1. Spinning disc apparatus (SDA)

Figure 1(*a*) shows a schematic of the deposit generation section in the SDA. A detailed description of the apparatus is given in Nigo *et al.* (2009). The apparatus consists of a cylindrical can partially immersed in a reservoir of test solution. Rotation is provided by a stepper motor. A recirculating water/glycol bath is used to regulate the temperature of the can, T_{cw}, whilst the temperature of the bulk solution, T_b, is maintained by a water jacket around the reservoir fed by a second, heating, recirculator. The can sides are insulated so that heat transfer occurs primarily through the base. A magnetic stirrer located at the base of the reservoir provides agitation and maintains temperature uniformity in the bulk solution. The temperature of the bulk solution, coolant and water jacket are monitored by T-type thermocouples connected to a datalogger.

Figure 1(*b*) shows the arrangement of the can base, which was used for heat transfer studies and fouling tests. A micro-foil heat flux sensor (Rhopoint, UK, type 27160) is located between a brass block and a removable 316 stainless-steel disc. The sensor was connected to a battery powered solid-state data collection unit located on the top of the can, so that data could be collected without the use of slip rings *etc.* and downloaded after an experiment. The thermal resistance of the combined plates and heat flux sensor, R_w, approximately 8.2×10^{-4} $m^2\,K\,W^{-1}$, is shown later to be small compared to the other terms.

2.2. Heat transfer tests

The surface temperature, T_s, is a key parameter in the fouling mechanism so a series of heat transfer tests were performed to characterize the thermal performance of the system. The same water/glycol mixture was used on the coolant side, in order to maintain coolant flow similarity. Liquid paraffin (the solvent in the fouling tests), 30 wt% and 78 wt% water/glycerol mixtures were used as the reservoir (bulk) liquid. These differed primarily in viscosity, so that a range of hydrodynamic conditions could be studied over the range of rotational speeds accessible with the stepper motor. The bulk liquid hydrodynamics were characterised by the Reynolds number, Re_r, defined as

$$Re_r = \frac{r_d^{\,2}\omega_d\rho_b}{\mu_b} \quad (1)$$

where, r_d, ω_d , μ_b and ρ_b are the disc radius, the angular velocity of the can, the dynamic viscosity and the density of the bulk solution, respectively. The viscosity was evaluated at the estimated surface temperature, T_s. The experimental conditions and bulk liquid properties are summarized in Table 1.

Heat transfer tests were performed with a charge of 2 L of liquid in the reservoir, as used in fouling tests. The can was initially isolated from the reservoir and coolant circulated to bring it to the required temperature. The data loggers were then activated, the can lowered into the bulk liquid and rotation started. The data reported are the values obtained after steady state was reached.

2.3. Model fat solutions

Test solutions were prepared by dissolving tripalmitin (PPP, >85% purity; density, 984 kg m^{-3}, Sigma Chemicals, UK) in liquid paraffin at 60 ºC to give solutions with composition 2.5, 5, 10, 20 and 50 wt%. All fouling tests reported here were performed with 5 wt% solutions. Solution composition was determined by gas chromatography (GC) on samples diluted in *n*-heptane (Hewlett Packard Agilent 6890 GC equipped with a dimethylpolysiloxane column, 10 m×0.32 mm×0.1 μm, and a flame ionisation detector using helium as the carrier gas). The GC was calibrated and programmed using the BS EN 14105:2003 method.

2.4. Cloud and melting points measurement

The cloud point of PPP solutions was measured under quasi-static conditions, where the only liquid motion was that provided by a magnetic stirrer. The cloud point, T_c, is the onset of spontaneous precipitation and was measured using a turbidity sensor (ODEON meter, NEOTEK-PONSEL, France). The turbidity probe was immersed in the sample held in a 50 mL jacketed beaker (4 cm in diameter and 6 cm in height) and stirred by a Teflon coated magnetic bar at low rotational speed. The sample temperature was measured using a T-type thermocouple and was initially held at 60 ºC for 10 min to eliminate any thermal history. The jacket liquid temperature was manipulated to lower the sample temperature at (*i*) 0.5 and (*ii*) 1.5 K min^{-1}. Turbidity was recorded at 10 s intervals and T_c taken as the temperature at which a significant and continuous rise in nephelometric turbidity units (NTU) was observed.

The melting point and melting enthalpy of samples was determined using a Perkin-Elmer Pyris 1 differential scanning calorimeter (DSC) fitted with a refrigerated cooling system. Scans were recorded from 0 to 80 ºC at heating and cooling rates of 10 K min^{-1}.

2.5. Rheological tests

A short rheological study was performed to investigate the effect of shear on the crystallisation of PPP from model solutions undergoing cooling. In the SDA the deposit gels are formed at a cold surface subject to shear. Samples of 5 wt% PPP solution were tested using serrated parallel plates on a Bohlin CV120 controlled stress rheometer (25 mm diameter, 0.1 mm gap). Temperature control was provided by a Peltier device located beneath the lower plate. The plates were preheated to 55 ºC before loading the sample and the sample was initially held at this temperature, at rest, for 10 min. The sample was then subjected to steady shear at a fixed shear stress of 2 Pa while subject to a temperature ramp of steady decrease from 55 to 5 ºC at 5 K min^{-1}, followed by 10 min at 5 ºC. The shear stress was set at 2 Pa in order to avoid shearing any developing microstructure severely while maintaining sufficient measurement accuracy. This shear stress is also representative of the shear stress exerted by the solution on the disc and deposit surfaces in fouling experiments.

2.6. Numerical simulation

Computational fluid dynamics simulation of the flow and temperature fields in the bulk liquid in the SDA were used to generate estimates of film heat transfer coefficient from the bulk liquid and the can base plate and the surface shear stress. These simulations can be performed with reasonable accuracy as the device is operated in the laminar flow regime and yield estimates of surface temperature and shear stress. The commercial finite element method software COMSOL Multiphysics (version 3.5, Chemical Engineering Module) was used to solve the continuity, Navier-Stokes and the steady state energy equations for a Newtonian liquid. The flow was modelled as being axisymmetric, incompressible, and steady state. Physical properties, such as density, thermal conductivity and specific heat capacity, were assumed not to change significantly with temperature and were assumed uniform throughout. This study extends the numerical simulation of Nigo *et al.* (2009), using similar boundary conditions but using modified fouling cell plate and quantitative settings to include a heat flux sensor and different base plate geometry. Moreover, the effect of thermal resistances from the coolant flow and combined plates were taken

into consideration to yield more accurate simulation results. The converged solution took approximately 15 min on a desktop PC with a 3.16 GHz dual core processor and 3.33 GB RAM.

2.7. Fat deposition studies

Deposition experiments reported here were performed in a 'cold start' mode, wherein the test surface and reservoir were initially brought to their respective operating temperatures by circulation of the heat transfer medium before the can was immersed in the bulk liquid and rotation started. This resulted in an initial transient where the test surface temperature increased from one close to that of the coolant liquid to an intermediate value. The transient was studied separately using PPP-free paraffin liquid and data reported later show that the transient lasted ~ 60 s. This cold start mode resulted in the formation of an initial gel layer but avoided transients associated with mixing if the PPP charge were added to the solution to start the fouling test. An alternative mode, of warm start, is under development and will be reported in due course.

The rotation speeds, ω_d, employed were 2.2, 3.5, 5.4 and 7.3 rad s^{-1}, corresponding to Re_r of 26, 41, 64 and 86, respectively. The cloud point of the 5 wt% solution was 29.8 ºC (at a cooling rate of 0.5 K min^{-1}) and coolant temperatures, T_{cw}, were selected to give a range of precipitation driving forces, namely 9.8 ºC (*i.e.* $T_c - 20$), 19.8 ºC ($T_c - 10$), 24.8 ºC ($T_c - 5$) and 29.8 ºC (T_c). Fouling tests normally lasted 12 h, but a series of interrupted tests were performed at one condition, for 1, 3, 6, 9 and 12 h, in order to establish reproducibility and to allow stages in deposit growth to be evaluated. The final deposit was removed from the surface using a plastic spatula, weighed and stored for further analysis.

2.8. Deposit analysis

The deposits consisted of gels of PPP crystals in a liquid matrix and contained PPP in the form of solids and entrained solution. The total PPP content, w_T, was determined by dissolving samples in a measured excess of *n*-heptane and measuring PPP content by GC as described above.

The solids content of the deposit, w_X, was determined by filtration. About 3 g of deposit was loaded on to a 0.2 μm polytetrafluoroethylene membrane filter paper (Cole-Parmer, USA) and vacuum applied. The filtered solids were washed with hexane (analytical reagent grade, Fisher Scientific, UK) at ambient temperature to remove any entrained paraffin followed by acetone to remove traces of hexane, then

allowed to dry at room temperature for an hour before weighing.

The rheology of the deposits was studied using a Bohlin CVO 120 controlled-stress rheometer operating in oscillatory testing mode as reported by Nigo *et al.* (2009) with the temperature of the bottom (stationary) plate set at 20 ºC. Tests were performed using roughened plates (top 25 mm diameter, base 50 mm diameter, gap 1 mm). The oscillating frequency was set at 10 rad s^{-1} (1.59 Hz) and the sample subjected to shear stress from 2.4 Pa to 29.3 kPa in an ascending ramp.

2.9. Statistical analysis

Analysis of variance (ANOVA) was applied and, when the effect of the factors was significant ($p < 0.05$), the Fisher least significant difference (test was used at 95% confidence level.

3. Results and discussion

3.1. Crystallisation under quiescent and shear conditions

Figure 2 summarises the melting and cloud point results for the model solutions of PPP in liquid paraffin and can serve as a simple crystallisation map. Both T_m and T_c decrease with decreasing PPP concentration, as expected. The melting point of the PPP melt (*i.e.* no paraffin added), at 65.4 ºC, compares favourably with the value of 66 ºC reported by Sato and Kuroda (1987). The enthalpy of melting, ΔH_{fp} of the PPP melt was 108 kJ mol^{-1}, which is lower than that obtained by Kellens *et al.* (1990), which was attributed to the differences in purity (165 kJ mol^{-1}, PPP ~ 99 % pure). The purer the sample, higher the enthalpy value as there are more PPP crystals per unit mass.

The T_m data in the Figure were fitted to the following solid-liquid equilibrium model for an ideal solution

$$\ln X_{PPP} = \frac{\Delta H_{fp}}{R}\left[\frac{1}{T_m^P} - \frac{1}{T_m}\right] \qquad (2)$$

where X_{PPP} is the mole fraction of PPP in solution, R is the universal gas constant, and T_m^P is the melting point of the pure component. The solutions were prepared with set mass fractions (as plotted in Figure 2) and the PPP mol fraction was estimated using relative molecular masses for PPP of 807.35 g mol^{-1} and 324 g mol^{-1} for paraffin (C_nH_{n+2}, where n = 23, from GC analysis). The ΔH_{fp} value obtained from the data fit, of 211 kJ mol^{-1}, differs noticeably from the DSC analysis, which can be attributed to impurities in the material and solvent-solute interactions (Davey and Garside, 2000).

The cloud points show a noticeable influence of cooling rate, with lower values observed for slower cooling rates, as discussed by Saiban and Brown (1997). The width of the metastable zone lay between 10 − 21 K of supercooling over the concentration range studied. The simple crystallisation map deduced from the study can serve as a guide to predict the likelihood of crystal formation at a given temperature and concentration. For the cold start operating mode employed in the experiments reported here, immersion of the cold test section in the warm solution at

313 the start of the experiment results in a high initial cooling rate: Figure 2 indicates that
314 this is likely to promote homogeneous nucleation and gel formation, as observed in
315 the experiments.
316
317 An example of crystallisation in the presence of shear is shown in Figure 3,
318 where a 5 wt% PPP solution sample was subjected to a steady shear stress of 2 Pa as it
319 was cooled from 55 to 5 ºC at 5 K min^{-1}. The T_m value for this solution under
320 quiescent conditions was measured at 49.1 ºC and the cloud point (at 0.5 K min^{-1}) was
321 29.8 ºC. The viscosity was calculated from the measured shear rate and is presented as
322 the relative viscosity, *i.e.* made dimensionless by division by the viscosity of the
323 paraffin solvent measured under similar conditions. The solution exhibits an initial
324 region, labelled A, in which the relative viscosity is close to unity, indicating the
325 absence of particles.
326
327 After about 7.5 minutes the relative viscosity increases markedly (region B),
328 corresponding to the appearance of crystals and formation of a suspension: the AB
329 transition marks the 'mechanical' cloud point. The sample temperature, at ~ 17 ºC, is
330 12 K lower than the quiescent T_c value. This is partly due to the turbidity meter
331 detecting the onset of cystallisation, *i.e.* a low number concentration of particles,
332 whereas the rheometer is sensitive to the formation of a network. The relative
333 viscosity increases by four decades, indicating the formation of a gel, which increases
334 in stiffness across region C as the solution continues to cool. The change in mass of
335 crystals in this region is small (compare the solubilities in Figure 2), indicating that
336 the change in viscosity is related to gel behaviour. A high viscosity plateau is reached
337 at ~ 10 ºC, where the peaks are indicative of wall slip and a network in the bulk phase.
338 These characteristics were confirmed by tests in a Linkam shear cell, a controlled
339 shear device fitted with observation windows. Similar transitions in fats have been
340 reported previously (De Graef *et al.*, 2009; Tarabukina *et al.*, 2009; Walstra *et al.*,
341 2001).
342
343 Figure 3 confirms that as the fat solution cools, once it starts to nucleate, it can
344 quickly form a highly viscous gel. The BC transition could be interpreted as a gelation
345 temperature. Comparing change in relative viscosity in region C with the solids
346 content estimated from the equilibrium locus in Figure 2 (data not reported) showed
347 the relative viscosity is not a simple function of the final solids content of gel,
348 indicating that the crystallisation under shear condition is under kinetic control.
349 Similar behaviour was observed with other PPP concentrations. Whilst this test does
350 not replicate the conditions on the SDA exactly, it does confirm that cold start

experiments will form gels rapidly, and that the first appearance of crystals is sensitive to shear and cooling conditions.

3.2. Heat transfer

Spinning disc devices are employed in mass transfer studies as the mass flux (and film mass transfer coefficient) does not vary with radial position across the surface. Sparrow and Gregg (1959) analysed the heat transfer behaviour of spinning discs operating in the laminar regime and showed that the heat flux, q, film heat transfer coefficient, h_b, and surface temperature, T_s, are similarly uniform. It should be noted that the laminar regime extends to Reynolds numbers of ~ 100,000. Measurements of the heat flux yield the overall heat transfer coefficient, U, defined as

$$q = U\left(T_b - T_{cw}\right) = h_b\left(T_b - T_s\right) \tag{3}$$

Writing U in terms of resistances in series yields

$$\frac{1}{U} = \frac{1}{h_b} + R_{cw} + R_w = \frac{1}{h_b} + R_{else} \tag{4}$$

where R_{cw} and R_w refer to the thermal resistance of the coolant flow and plates, respectively, and are lumped together as R_{else}. The h_b term is expected to follow a dependency of the form (Sparrow and Gregg, 1959);

$$Nu \equiv \frac{h_b r_d}{k_b} = aRe_r^{\,0.5} Pr^{1/3} \tag{5}$$

where Nu is the Nusselt number based on the disc radius, k_b the thermal conductivity of the bulk liquid, Pr its Prandtl number and the parameter a is a constant. Equation (5) suggests that the data obtained for different liquids should follow similar behaviour when plotted as $Nu/Pr^{1/3}$ against Re_r. The film heat transfer coefficient is not directly accessible, however, and some estimation is required.

An alternative Nusselt number, Nu^*, can be based on U and its relationship to Nu given by Equation (4):

$$Nu^* \equiv \frac{U r_d}{k_b} = \frac{Nu}{1 + R_{else} h_b} \tag{6}$$

Inspection shows that at low Re_r, when h_b is small and is expected to influence heat transfer strongly, $Nu^* \sim Nu$ and the dependency on Re_r is expected to mirror Equation (5). At larger values of Re_r, Equation (6) indicates that Nu^* is likely to give a poorer estimate of h_b. This is confirmed by Figure 4, where the heat transfer dependency on Re_r (Equation (5)) starts to differ from the trend in the data at higher Re_r. Nu^* differs noticeably from Nu estimated using Equation (5) with a = 0.62, indicating that the parameter a required modification, which was achieved by simulation (next section).

The above analysis assumes that R_w does not vary strongly with rotation speed, which is considered reasonable because of turbulence in the coolant flow geometry and the influence of constant, conduction contributions. The thermal resistance of coolant side, R_{cw}, in the SDA system becomes more significant as Re_r is increased and this is estimated by difference, as outlined below.

3.3. CFD simulations

The CFD simulations yield predictions of velocity and temperature distributions in the bulk liquid in the heat transfer experiments. The coolant flow is not modelled: its contribution is expressed as a uniform film heat transfer coefficient. Figure 5 shows the stream functions (contour lines) and the temperature profiles (coloured background) obtained for one of the sets of conditions employed in deposition tests. Two vortices are evident in the bulk liquid: an upper one driven by the rotation of the disc, and a lower one induced by the magnetic stirrer acting in the opposite direction.

Simulations were run for a set of cases covering the experimental conditions reported in Figure 4 and values of h_b extracted from the simulations. R_{else} is then estimated from $(1/U - 1/h_b)$ and R_{cw}, the thermal resistance on the coolant side, is then evaluated from $(R_{cw} - R_w)$. The static resistance associated with the base plates, R_w, is constant over the range of temperatures considered here. A subset of the results related to deposition testing are presented in Figure 6. The film resistance $1/h_b$ decreases with increasing Re_r, as predicted by the correlation (Equation (5)), and the simulation values show good agreement with the correlation: fitting the data to a power law trend yielded a power law index of 0.48, in good agreement with the value of 0.50 in Equation (5). R_{cw} also decreases with rotation speed, and is consistently smaller than $1/h_b$, indicating that the dominant resistance to heat transfer lies on the bulk (fat) side.

These results allow T_s to be estimated by combining Equations (3) and (4), *viz.*

$$T_s(t) = T_b - \frac{q}{h_b} = T_b - \left[\frac{T_b - T_{cw}}{R_{cw} + R_w + R_f(t) + \frac{1}{h_b}} \right] \frac{1}{h_b} \tag{7}$$

where R_f is the thermal resistance of any fouling layer. Assuming that the other resistances do not vary with temperature as fouling develops allows R_f to be evaluated from

$$R_f(t) = \frac{1}{U(t)} - \frac{1}{U_0} \tag{8}$$

where U_0 is the initial, clean, overall heat transfer coefficient. Similarly, the temperature at the base plate/deposit interface, T_w (= T_s when R_f = 0) can be evaluated from

$$T_w(t) = T_{cw} + q\left(R_{cw} + R_w\right) \tag{9}$$

Figure 7(*a*) shows the initial, clean, steady state T_s at over the range of T_{cw} and ω_d of interest. The plots show that T_s is more sensitive to T_{cw}. A key assumption in these estimates is that the release of enthalpy of crystallisation during deposition is negligible: this is considered further in Section 3.5.

The average shear stress imposed on the disc surface can also be calculated from the simulated velocity field. The shear stress is directly proportional to radial position, *r*, and Figure 7(*b*) shows the average wall shear stress calculated at *r* from 0 to 0.035 m. The CFD calculations indicate that the average shear stress is of the order of 0.3 – 2.3 Pa for the initial clean surface. This compares favourably with the range of surface shear stresses reported by Fitzgerald *et al.* (2004) using a rectangular duct flow cell, of 0.5 – 4.0 Pa. Larger shear stresses could be obtained in the SDA using a different motor. Since surface temperature and shear stress are key parameters in freezing fouling, Figure 7 illustrates the range of surface conditions that can be investigated in deposition studies.

3.4. Fouling Profiles

The reproducibility of the fouling test was confirmed by conducting a series of experiments under identical conditions for various times. The R_f - *t* plots in Figure 8 show good agreement, with a maximum difference of 3%. Subsequent tests were repeated only when the results were inconsistent with observed trends. These interrupted tests also allowed the evolution of deposit properties to be investigated.

The R_f - *t* plots obtained in the 'cold start' experiments discussed here all showed similar behaviour, exhibiting three stages:

(*i*) an initial step in R_f,

(*ii*) a period of linear increase in R_f, followed by

(*iii*) a falling rate period, where R_f approaches an asymptote.

The initial sharp increase in R_f derives from the cold start mode. On immersion of the test cell, the warm solution is contacted with the cold surface (below T_c), inducing gel formation. At the same time, the heat flow through the cell is larger than at steady

state owing to the transient in heat conduction, resulting in a temporally large heat flux and associated U value. The definition of R_f in Equation (8) means that there is a transient, with negative R_f values, as shown in Figure 9. The Figure shows that a thermal steady state was reached within 2 min, by which time a gel layer had been established. Figure 9 also shows the transient observed under identical conditions with paraffin alone, in which case no gel is formed and the steady state R_f value is zero. Negative values of R_f associated with roughness enhancing convective heat transfer have been reported by other workers, *e.g.* Crittenden and Khater (1987); Bansal and Müller-Steinhagen (1993), but this transient mechanism is rarely reported, mainly because the experiments start with heat transfer in steady state. The initial step in R_f was reproducible (see Figure 8(*a*)), and decreased as the coolant temperature increased (Section 3.8).

In the subsequent stages, as deposit accumulates, the deposit-solution interface temperature, T_s, increases and the wall temperature, T_w, decreases. The calculated values of T_s and T_w in Figure 8(*b*) show a rapid increase in T_s which slows down following the linear fouling stage and approaches an asymptote, which is close to T_m. T_s is not measured directly, so there is some uncertainty in the estimate. Tests under other conditions showed similar behaviour. Figure 8(*b*) shows a moderate decrease in wall temperature over time, which would promote further crystallisation of the gel. It is noteworthy that the end of the linear fouling regime, at a temperature denoted $T_s = T^*$ (estimated by eye as the end of the linear region), extends beyond the point where $T_s = T_c$ (here, T_c = 29.8 ºC at 0.5 K min^{-1}, reached after ~ 50 min). The controlling mechanism does not, therefore, appear to be crystallisation at the deposit interface, with $T_s = T_c$, as reported by Singh *et al.* (2000).

The R_f - m data from all experiments reported in this study are plotted Figure 10. When deposition is uniform, the relationship between R_f and the mass of deposit per unit disc surface, m, is;

$$R_f = \frac{m}{\rho_f k_f} \qquad (10)$$

where ρ_f is the deposit density. The deposit thermal conductivity, k_f, was taken to be 0.15 W m^{-1} K^{-1}, as the thermal conductivity of solid PPP is conveniently close to that of paraffin. The Figure shows a linear relationship (R^2 = 0.97), in good agreement with Equation (10). The gradient, of 0.011 m^4 K W^{-1} kg^{-1}, yields an estimate of $\rho_f k_f$ = 91 W kg m^{-4} K^{-1}, which is lower than the value expected for the paraffin, of 130.5 W kg m^{-4} K^{-1} $\rho_f k_f$ (Fitzgerald *et al.*, 2004) for the PPP solids will be greater again. The difference may be due to the difficulty in collecting all the deposit (affecting m), and

any systematic errors in evaluating R_f. The linear relationship does, moreover, indicate that the age of the deposit does not affect heat transfer. It is worth noting that the linear relationship of the R_f - m data obtained by the interrupted tests (Figure 8) indicates that the heat flux measurements provided a reliable monitor of deposit growth.

The deposit composition data in Figure 11 exhibit a noticeable change over the course of the 12 h fouling test. The solids fraction, labelled w_X, increased almost linearly to about 15 wt% over the first 6 h, coinciding with the linear increase in R_f. The subsequent change in w_X was less marked, reaching 20 wt% after 12 h. The composition of the liquid phase within the deposit, w_S, is calculated from the measured values of w_T (GC) and w_X (filtration) via;

$$w_S = \frac{w_T - w_X}{1 - w_X} \tag{11}$$

The data in Figure 11 show w_S being similar to that of the bulk liquid, and increasing over time to ~ 10 wt%. The increase in w_S is less marked than that observed in w_X, and the enrichment in solution composition (increase in w_S) after 6 h was not statistically significant. These data indicate that the deposit undergoes ageing, mainly through increasing solids content. Further crystallisation of PPP from the solution trapped in the deposit as the local temperature decreases (see Figure 8(*b*)) would tend to reduce the concentration of PPP in solution. Higher resolution measurements are required to confirm whether the solution is being enriched, which would require diffusion into the deposit from the bulk solution.

One explanation for the increase in solids content is shear-induced hardening. The latter is related to the shear stress imposed on the surface, which is controlled by ω_d, and liquid properties (principally T_s). As fouling continues, T_s increases, the viscosity decreases and the solids composition required to form a gel strong enough to resist deformation by the surface shear stress will increase. These competing aspects of temperature have been reported for wax formation in crude oils by Bansal and Müller-Steinhagen (1993). Shear hardening would not require w_S to increase. However, in these tests, the change in T_s also reduces the shear stress imposed by the bulk liquid. Decoupling these factors and establishing the driving force for ageing is the subject of ongoing work, including imaging of the deposits.

3.5. Fouling mechanisms

R_f - t profiles featuring falling rate and asymptotic behaviour are often fitted to the

Kern-Seaton model based on competing deposition and removal processes, *viz.*

$$R_f = R_f^* \left[1 - \exp\left(-t / t_F\right)\right] \quad (12)$$

where R_f^* is the asymptotic fouling resistance and t_F is a characteristic time, which can be related to initial fouling rate via $[dR_f/dt]_{t=0} = R_f^*/t_F$. This approach has been applied to wax formation from oils by Nazar *et al.* (2005), Akbarzadeh and Zougari (2008) and Ramirez-Jaramillo *et al.* (2010) but is not appropriate here as (*a*) the initial linear regime is not consistent with the model; (*b*) fitting the R_f - t profiles to Equation (12) gave systematic deviations in fitting; and (*c*) the asymptotic level, R_f^*, is related to T_m, rather than a removal step. It is noteworthy that no removal was observed in these tests. Fitzgerald *et al.* (2004) also reported initial, linear fouling behaviour followed by falling rate behaviour but this was interrupted by spalling, which was not observed in these tests. Future work will consider higher rotation rates to see if this can induce spalling in these deposits.

The estimates of R_f, surface and wall temperatures reported here assume that the enthalpy released on forming the deposit, *i.e.* from PPP crystallisation, is small compared to the total rate of heat transfer. The heat flux sensor measures the rate of heat transfer to the coolant, so if the rate of latent heat evolution were significant, the rate of convective heat transfer would be less than the measured value: Equation (3) indicates that a lower q would result in higher T_s. The contribution from latent and sensible heat effects on heat transfer was therefore considered by comparing the enthalpy associated with forming the deposit with the total amount of thermal energy transferred through the heat flux sensor over the course of a 12 h fouling test.

The enthalpy of crystallisation associated with the crystals in the deposit, H_X, was estimated from

$$H_X = m w_X \Delta H_{fp} \quad (13)$$

where m and w_X are the measured deposit mass coverage and solids fraction, respectively, taken from Figures 10 and 11. The latent heat of crystallisation was taken as 211 kJ mol^{-1} (Section 3.1), which is a worst case estimate as the true value is likely to be smaller, nearer 100 kJ mol^{-1}. The sensible heat associated with the deposit was estimated from

$$H_S = m C_p \left[T_b - \tfrac{1}{2}\left(T_s + T_w\right)\right] \quad (14)$$

This estimate assumes that the deposit has uniform heat capacity, C_p, taken as that of the paraffin, and a linear temperature distribution across the deposit. Figure 12 shows

557 that H_S was initially the dominant contribution, with H_X increasing in importance over
558 time, but the combined contribution ($H_O = H_X + H_S$) was consistently small, at 1 − 2
559 % of the total amount of thermal energy transferred. Neglecting latent heat effects in
560 estimating R_f therefore appears reasonable.
561

562 *3.6. Growth rates*

563 The above calculation indicates that heat transfer was not determining the rate of
564 deposit formation. Further insight into the mechanisms involved can be obtained by
565 comparing the observed deposit growth rate with one estimated from the maximum
566 rate of mass transfer of PPP to the surface. The 5 wt% solutions can be considered
567 dilute (the mole fraction of PPP in the bulk solution is ~ 0.02): the mass flux, N_{PPP},
568 from the bulk solution with PPP concentration, x_b, towards the surface where growth
569 occurs (with local concentration, x_s) can be estimated from

570 $$N_{PPP} = k_m\left(x_b - x_s\right) \tag{15}$$

571 where k_m is the film mass transfer coefficient, and x_i is a mass concentration (in kg
572 m^{-3}). The maximum flux was estimated by setting the concentration at the surface, x_s,
573 to be that in equilibrium with solid PPP at the surface temperature, T_s (*i.e.* rapid
574 crystallisation). The rate of deposition, N_d, can then be estimated from the solids
575 content of the layer, w_X, via

576 $$N_d = \frac{k_m}{w_X}\left(x_b - x_s\right) \tag{16}$$

577 Gregory and Riddiford (1956) reported the following expression for k_m for a disc
578 rotating in an infinite Newtonian fluid;

579 $$k_m = 0.62\frac{D}{r_d}Re_r^{1/2}Sc^{1/3} \tag{17}$$

580 where *Sc* is the Schmidt number, expressed as;

581 $$Sc = \frac{\mu_b}{\rho_b D} \tag{18}$$

582 Here *D* is diffusivity of solute in solvent, which was estimated from the Wilke and
583 Chang correlation (1955) to lie in the range of $4 - 17\times10^{-11}$ m^2 s^{-1} for the PPP/paraffin
584 solutions employed here. Calculation of N_d requires evaluation of the transport
585 parameters and x_s, and hence the surface temperature: T_s was calculated at selected
586 times using Equation (7) and the experimental R_f value.

587

588 The actual deposition rate was estimated from the thickness growth rate, G, by N_d
589 = $\rho_f G$. The thickness growth rate, G, was calculated from the R_f measurements by
590 assuming the deposit thickness, δ_f, to be uniform and k_f known, via;

591 $$G = \frac{d\delta}{dt} = k_f \frac{dR_f}{dt} \quad (19)$$

592 The gradient dR_f/dt (and also the surface temperature, T_s) were evaluated by
593 interpolating the R_f and T_s data sets and extracting values at particular points.
594
595 Figure 13 shows the rates calculated for the 12 h fouling experiment in Figure 8.
596 Over the first 300 min, where linear fouling was observed, the deposition rate
597 calculated from the R_f data was considerably smaller than the maximum PPP mass
598 flux, indicating that fouling was not controlled by mass transfer in this regime. The
599 mechanism remains to be determined, as the subsequent studies of temperature and
600 velocity show the fouling rate to be relatively insensitive to these parameters.
601
602 In the falling rate regime the actual deposition rate is close to N_d estimated by
603 this simple mass transfer model. The main reason for the variation in N_d over time in
604 Figure 13 is the change in $(x_b - x_s)$ with T_s, and in the falling rate regime this could be
605 attributed to mass transfer or crystallisation effects.
606
607 The transition from linear to falling rate fouling behaviour indicates a change in
608 growth mechanism and this section considers the latter phase. No particulates were
609 present in the bulk solution, and inspection of Figures 8(*a*) and (*b*) suggest that the
610 growth rate in this phase is related to the surface temperature and the temperature
611 driving force ΔT, the latter being defined as the difference between T_m and the
612 temperature of crystallisation, here T_s. T_s (and thence ΔT) in the falling rate stage was
613 estimated by interpolating the R_f and T_s data sets as described above and extracting
614 values at particular points. Figure 14 shows the results obtained for the runs in Figure
615 8. A linear trend is evident, which is the form expected for normal growth (Borisov *et*
616 *al.*, 1968):

617 $$G = K\Delta T \quad (20)$$

618 The fitted line does not pass through the origin, which is attributed to the systematic
619 uncertainties involved in calculating T_s from the experimental data.

3.7. Effect of velocity

The effect of velocity was studied at four rotational speeds, corresponding to average shear stresses on the disc surface of 0.26, 0.52, 1.03 and 1.66 Pa. Figure 15 presents the R_f - t profiles obtained from experiments performed at T_b = 60 ºC and T_{cw} = 9.8 ºC for 12 h. Under these conditions the test section surface temperature increases with ω_d, since h_b is more sensitive to ω_d than R_{cw}. The three stages described previously are evident in each case. The initial step increase in R_f decreased as ω_d increased. This may occur because the incipient gel is relatively weak, and was less able to resist the shear forces imposed on it at higher ω_d, or because the new, steady state temperature was warmer at higher ω_d (Equation (7)).

The linear fouling rate did not change appreciably with ω_d, varying from 1.21×10^{-6} to 1.32×10^{-6} m^2 K J^{-1}. Inspection of the (estimated) T_s - t plots indicated that the end of the linear fouling stage occurred at similar values of T_s, around 45.7 ºC (*i.e.* T_m – 4.6 K). After this point, the fouling rate exhibited normal growth kinetics with K value of $1 - 2\times10^{-5}$ μm s^{-1} K^{-1} and T_s approaching T_m as discussed above.

The fouling resistance, R_f, reached after 12 h decreased with increasing ω_d. The associated mass of deposit (m, Figure 16) was similarly reduced, and the plot of R_f against m in Figure 10 indicates that the deposit properties were similar to those reported above. The deposit composition data in Figure 16 show no effect of ω_d on w_S: the variation in w_S lies within the confidence limits for the hypothesis that the value is the same for all cases. The solids content, w_X, however increases noticeably with ω_d, by a factor of $3 - 4\times$ over the range studied. This result is consistent with the formation of a stiffer deposit to withstand the higher shear stress conditions present at its formation. An alternate explanation, given by Jennings and Weispfennig (2005), is that the thinner gel (smaller δ_f) and higher h_b result in a larger temperature gradient across the deposit, creating a higher diffusive flux for hardening. Again, detailed microstructural distribution data are required to elucidate this behaviour.

3.8. Effect of thermal driving force

Figure 17 shows the effect of thermal driving force for tests performed at ω_d = 5.4 rad s^{-1} at four different coolant temperatures. The initial degree of subcooling (T_c – T_{cw}) ranged from 20 K to zero, based on T_c measured at a cooling rate of 0.5 K min^{-1}. The R_f - t profiles again exhibit the three stages mentioned above. The initial step

increase is larger and the final R_f value higher with increased subcooling (lower T_{cw}), as expected. It is noteworthy that an initial gel layer is formed at zero subcooling, indicating that the cloud point calculated under quasi-static conditions does not map directly to deposition tendency in these systems. For comparison, the initial cooling rate in the paraffin in Figure 9 is of the order of 37 K min^{-1}, and the true cloud point would thus be raised significantly by the rapid cooling rate.

The amount of deposit also increased with the degree of subcooling, and Figure 18(*a*) suggests a strongly linear relationship. This extrapolated locus continues beyond T_c, and suggests that no deposition would occur when $T_{cw} \sim 40$ ºC. Tests with $T_{cw} > T_c$ were not performed here. Another factor which may play a role is the presence of the stainless steel surface, which could promote monolayer formation (and heterogeneous nucleation and growth) at temperatures above the bulk cloud point (for homogeneous nucleation).

The linear fouling stage was shorter as T_{cw} increased, which is consistent with less time elapsing before the transition temperature – again, around 46.1 ºC – was reached. The linear fouling rates were similar to those reported above, ranging from 1.04×10^{-6} to 1.21×10^{-6} m^2 K J^{-1}. Falling rate fouling could again be described by Equation (20), with K values of $1 - 2\times10^{-5}$ μm s^{-1} K^{-1}.

The deposit composition data in Figure 18(*b*) again show little effect of subcooling on PPP concentration in the liquid entrained in the deposit. The values are consistently larger than the bulk concentration, but the uncertainty in the measurement increases with reduced subscooling. The solids mass fraction data exhibit a twofold difference over the T_{cw} range studied, increasing with lower initial subcooling (and most of the growth occurring via normal crystallisation). Visual inspection of the deposits indicated that for this fixed shear rate, those formed under conditions of smaller subcooling were firmer. The deposits formed under high subcooling conditions (and faster initial rate) appear to incorporate more solution, which could either be due to a growth occurring via a dendritic front or the effect of higher liquid viscosity at lower temperature. Singh *et al.* (2001a) also reported higher liquid contents in wax deposit formation at higher subcoolings.

3.9. Deposit rheology

The strength of the gels formed was investigated by oscillatory rheometry. Shear stress sweeps were performed at a frequency of 1.59 Hz. The results obtained for

690 many of the deposits obtained from the fouling tests described above are presented in
691 Figure 19. The rheological parameters extracted are those reported by Nigo *et al.*
692 (2009): the elastic modulus in the linear elastic region, G', the limit of linearity, τ_{EL},
693 defined as the end of the linear elastic region, where G' deviated more than 5% from
694 its initial value, and τ_C, the crossover point of elastic and viscous moduli. It is
695 noteworthy that all the τ_C values are > 2 Pa, the maximum surface shear stress
696 estimated in the SDA tests reported here. The Figure shows that all the parameters
697 increased with solids volume fraction in a strongly non-linear manner, and there is
698 good overlap with the data reported by Nigo *et al.* (2009) for similar materials.
699
700 As a particulate soft solid, the rheological parameters are expected to be strongly
701 determined by the solid volume fraction in the gel, ϕ. The data exhibit power-law
702 behaviour and could be fitted to the form:

703 $$Y = b\phi^n \qquad (21)$$

704 where Y is the rheological parameter and b and n are positive constants. The gels are
705 then consistent with the fractal model (Tang and Marangoni, 2007), where b and n are
706 constants related to structural characteristics of the fat crystal network. In that model,
707 the structure of a colloidal network is considered as a collection of fractal flocs, the
708 increase of G', τ_{EL} and τ_C with ϕ can be explained by the increase in the number of
709 interfloc links with solid fat content (Marangoni and Rogers, 2003; Shih *et al.*, 1990;
710 Venkatesan *et al.*, 2005). The results show that the gel quickly developed an
711 appreciable strength, so that it would resist the shear imposed by the fluid over the
712 surface. However, it was not possible here to determine the local solids distribution:
713 this will be investigated using freezing techniques.

714

4. Conclusions

The SDA allows one to investigate the heat and mass transfer characteristics of gel formation from model food fat solutions on cold surfaces under well controlled flow conditions. Experimental investigations of the SDA heat transfer performance were combined with CFD simulation studies to generate maps of the temperature and shear stress conditions on the SDA test surface. The results confirmed that the thermal resistance across the disc was small and heat transfer was controlled by the bulk fluid, however, the internal thermal resistances became significant at higher Re_r.

A series of laboratory experiments were carried out in the SDA with 5 wt% PPP in a non-crystallising solvent to investigate the effects of varying deposition time, shear and thermal driving force on the crystallisation fouling behaviour of food fats. R_f - t profiles for these 'cold start' experiments exhibited three stages: transient, linear rate and falling rate stage. R_f - t profiles could be generated reliably and reproducibly, indicating that the heat flux measurements provide a reliable monitor of deposit growth. In all cases, the H_X contribution in H_T is noticeably small, the estimated T_s increased quickly initially and then levelled off to approach the experimentally measured T_m.

The amount of gel formed initially could be related to the subcooling of the cold disc. The linear fouling rate was relatively insensitive to temperature and velocity effects and the rate controlling step is yet to be identified. In the falling rate stage, the observed dependence of $G(T)$ on ΔT was linear, regardless of the operating conditions, indicating that a normal growth stage controls fouling at these temperatures.

For given values of ω_d and T_{cw}, m and w_X increased steadily with t, indicating that deposit ageing occurred in the gels over the time scale of the experiments. Ageing did not change the deposit properties in terms of $\rho_f k_f$. The strength of the gel formed, whether described by G', τ_{EL} or τ_C, increased with solids content and could be related to a fractal model of deposit microstructure.

At the shear and temperature conditions employed in this study, deposition is driven by formation of gels on the heat transfer surface. The composition and structure of the gels reflected the conditions present at their formation. Increasing the amount of shear generally decreased m and increased w_X, while decreasing the coolant temperature (and increasing the degree of subcooling) increased m and decreased w_X. Spalling was not observed under the moderate shear stress conditions studied here.

Nomenclature

Roman

a	constant in Equation 5
b	constant in Equation 21
C_p	deposit heat capacity, J kg^{-1} K^{-1}
D	diffusivity of solute in solvent, m^2 s^{-1}
G	growth rate of deposit thickness, μm s^{-1}
G'	elastic modulus in linear region, Pa
h_b	film heat transfer coefficient in bulk fluid, W m^{-2} K^{-1}
H_O	combined contribution of H_X and H_T, J or kJ
H_S	sensible heat associated with the deposit, J or kJ
H_T	total heat energy transferred during fouling run, J or kJ
H_X	latent heat of PPP crystallisation, J or kJ
ΔH_{fp}	melting enthalpy of PPP, J mol^{-1}
k_b	liquid thermal conductivity, W m^{-1} K^{-1}
k_f	deposit thermal conductivity, W m^{-1} K^{-1}
k_m	film mass transfer coefficient of bulk solution, m s^{-1}
K	constant in Equation 20, μm s^{-1} K^{-1}
m	mass of deposit per unit disc surface, kg m^{-2}
n	constant in Equation 21
N_d	deposition rate, kg m^{-2} s^{-1}
N_{PPP}	mass flux of PPP towards surface, kg m^{-2} s^{-1}
Nu	Nusselt number, -
Nu^*	modified Nusselt number, -
Pr	Prandtl number, -
q	heat flux, W m^{-2}
r	radial position, m
r_d	disc radius, m
R	universal gas constant, J kg^{-1} K^{-1}
R_{cw}	thermal resistance of coolant side, m^2 K W^{-1}
R_f	fouling resistance, m^2 K W^{-1}
R_f^*	asymptotic fouling resistance, m^2 K W^{-1}
R_w	thermal resistance of disc wall, m^2 K W^{-1}
R_{else}	thermal resistance of coolant flow and plates, m^2 K W^{-1}
Re_r	Reynolds number of bulk solution, -
Sc	Schmidt number, -
t	deposition time, s, min or hr
t^*	end time of linear fouling rate regime, s

787 t_F characteristic time, s, min or hr
788 T^* surface temperature at the end of linear fouling rate region, ^oC or K
789 T_b bulk temperature, ^oC or K
790 T_c cloud point, ^oC or K
791 T_{cw} coolant temperature, ^oC or K
792 T_m melting point, ^oC or K
793 T_m^P melting point of pure PPP, ^oC or K
794 T_s deposit surface temperature, ^oC or K
795 T_w temperature at base plate/deposit interface, ^oC or K
796 ΔT difference between T_m and T_s, K
797 U overall heat transfer coefficient, W m^{-2} k^{-1}
798 U_0 initial value of U, W m^{-2} K^{-1}
799 w_X solids content in deposit, wt%
800 w_S PPP content in the solution entrained in deposit, wt%
801 w_T total PPP content in deposit, wt%
802 x_b PPP concentration in bulk solution, kg m^{-3}
803 x_s PPP concentration at surface, kg m^{-3}
804 X_{PPP} mole fraction of PPP in solution, -
805 Y rheological parameters G', τ_C and τ_{EL}
806 *Greek*
807 δ_f deposit thickness, μm
808 μ_b apparent viscosity of bulk fluid, kg m^{-1} s^{-1}
809 ρ_b density of bulk fluid, kg m^{-3}
810 ρ_f deposit density, kg m^{-3}
811 τ_C crossover point of elastic and viscous modulus, Pa
812 τ_{EL} the end point of the linear region, Pa
813 ϕ solids volume fraction of deposit, %
814 ω_d can rotational speed, rad s^{-1}
815
816 *Abbreviations*
817 CFD computational fluid dynamics
818 DSC differential scanning calorimeter
819 NTU number of turbidity units
820 PPP tripalmitin
821 SDA scanning disc apparatus

References

Akbarzadeh, K., Zougari, M., (2008). Introduction to a novel approach for modeling wax deposition in fluid flows. 1. Taylor-Couette system. Industrial & Engineering Chemistry Research 47(3), 953-963.

Bansal, B., Muller-Steinhagen, H., (1993). Crystallization Fouling in Plate Heat Exchangers. Journal of Heat Transfer 115(3), 584-591.

Bidmus, H.O., Mehrotra, A.K., (2004). Heat-transfer analogy for wax deposition from paraffinic mixtures. Industrial & Engineering Chemistry Research 43(3), 791-803.

Borisov, V.T., Dukhin, A.I., Matveev, Y.E., Nikonova, V.V., Rakhmanova, E.P., (1968). Kinetics of crystallisation and mechanism of crystal growth in metallic systems. Journal of Crystal Growth 3-4, 663-665.

Crittenden, B.D., Khater, E.M.H., (1987). Fouling From Vaporizing Kerosine. Journal of Heat Transfer 109(3), 583-589.

Davey, R., Garside, J., (2000). Phase equilibria and crystallization techniques, in: Davey, R., Garside, J. (Eds.), *From molecules to crystallizers*. Oxford University Press, Oxford, UK, pp. 6-14.

De Graef, V., van Puyvelde, P., Goderis, B., Dewettinck, K., (2009). Influence of shear flow on polymorphic behavior and microstructural development during palm oil crystallization. European Journal of Lipid Science and Technology 111(3), 290-302.

Elphingstone, J.G.M., Greenhill, K.L., Hsu, J.J.C., (1999). Modeling of Multiphase Wax Deposition. Journal of Energy Resources Technology 121(2), 81-85.

Epstein, N., (1983). Thinking about heat transfer fouling: A 5 x 5 matrix. Heat Transfer Engineering 4(1), 43 - 56.

Fernandez-Torres, M.J., Fitzgerald, A.M., Paterson, W.R., Wilson, D.I., (2001). A theoretical study of freezing fouling: limiting behaviour based on a heat and mass transfer analysis. Chemical Engineering and Processing 40(4), 335-344.

Fitzgerald, A.M., Barnes, J., Smart, I., Wilson, D.I., (2004). A model experimental study of coring by palm oil fats in distribution lines. Food and Bioproducts Processing 82(3), 207-212.

852 Gregory, D.P., Riddiford, A.C., (1956). Transport to the surface of a rotating disc.
853 Journal of the Chemical Society(OCT), 3756-3764.

854 Hartel, R.W., (2001). *Crystallization in Foods*. Aspen Publication, Maryland, USA.

855 Hillig, W.B., (1966). A derivation of classical two-dimensional nucleation kinetics
856 and the associated crystal growth laws. Acta Metallurgica 14(12), 1868-1869.

857 Hillig, W.B., Turnbull, D., (1956). Theory of crystal growth in undercooled pure
858 liquids. Journal of Chemical Physics 24(4), 914.

859 Jackson, K.A., Chalmers, B., (1956). KINETICS OF SOLIDIFICATION.
860 Canadian Journal of Physics 34(5), 473-490.

861 Jennings, D.W., Weispfennig, K., (2005). Effects of shear and temperature on wax
862 deposition: Coldfinger investigation with a Gulf of Mexico crude oil. Energy and
863 Fuels 19(4), 1376-1386.

864 Kellens, M., Meeussen, W., Reynaers, H., (1990). Crystallization and phase-transition
865 studies of tripalmitin. Chemistry and Physics of Lipids 55(2), 163-178.

866 Kern, D.Q., Seaton, R.E., (1959). A theoretical analysis of thermal surface fouling.
867 British Chemical Engineering 4(5), 258-262.

868 Marangoni, A.G., Rogers, M.A., (2003). Structural basis for the yield stress in plastic
869 disperse systems. Applied Physics Letters 82(19), 3239-3241.

870 Mullin, J.W., (1993). *Crystallisation* (3rd Edition ed). Butterworth-Heinemann,
871 London, UK.

872 Nazar, A.R.S., Dabir, B., Islam, M.R., (2005). Experimental and Mathematical
873 Modeling of Wax Deposition and Propagation in Pipes Transporting Crude Oil.
874 Energy Sources 27(1-2), 185.

875 Nigo, R.Y., Chew, Y.M.J., Houghton, N.E., Paterson, W.R., Wilson, D.I., (2009).
876 Experimental studies of freezing fouling of model food fat solutions using a novel
877 spinning disc apparatus. Energy & Fuels 23(12), 6131-6145.

878 Parthasarathi, P., Mehrotra, A.K., (2005). Solids deposition from multicomponent
879 wax-solvent mixtures in a benchscale flow-loop apparatus with heat transfer.
880 Energy and Fuels 19(4), 1387-1398.

881 Ramirez-Jaramillo, E., del Rio, J.M., Manero, O., Lira-Galeana, C., (2010). Effect of
882 Deposition Geometry on Multiphase Flow of Wells Producing Asphaltenic and
883 Waxy Oil Mixtures. Industrial & Engineering Chemistry Research 49(7),

884 3391-3402.

885 Ribeiro, F.S., Souza Mendes, P.R., Braga, S.L., (1997). Obstruction of pipelines due
886 to paraffin deposition during the flow of crude oils. International Journal of Heat
887 and Mass Transfer 40(18), 4319-4328.

888 Saiban, S., Brown, T.C., (1997). Kinetic model for cloud-point blending of diesel
889 fuels. Fuel 76(14-15), 1417-1423.

890 Sato, K., Kuroda, T., (1987). Kinetics of melt crystallization and transformation of
891 tripalmitin polymorphs. Journal of the American Oil Chemists' Society 64(1),
892 124-127.

893 Shih, W.-H., Shih, W.Y., Kim, S.-I., Liu, J., Aksay, I.A., (1990). Scaling behavior of
894 the elastic properties of colloidal gels. Physical Review A 42(8), 4772.

895 Singh, P., Venkatesan, R., Fogler, H.S., Nagarajan, N., (2000). Formation and aging
896 of incipient thin film wax-oil gels. AIChE Journal 46(5), 1059-1074.

897 Singh, P., Venkatesan, R., Fogler, H.S., Nagarajan, N.R., (2001a). Morphological
898 evolution of thick wax deposits during aging. AIChE Journal 47(1), 6-18.

899 Singh, P., Youyen, A., Fogler, H.S., (2001b). Existence of a critical carbon number in
900 the aging of a wax-oil gel. AIChE Journal 47(9), 2111-2124.

901 Sparrow, E.M., Gregg, J.L., (1959). Heat transfer from a rotating disk to fluids at any
902 Prandtl number. Journal of Heat Transfer 81, 249-251.

903 Tang, D., Marangoni, A.G., (2007). Modeling the rheological properties and structure
904 of colloidal fat crystal networks. Trends in Food Science & Technology 18(9),
905 474-483.

906 Tarabukina, E., Jego, F., Haudin, J.M., Navard, P., Peuvrel-Disdier, E., (2009). Effect
907 of shear on the rheology and crystallization of palm oil. Journal of Food Science
908 74(8), E405-E416.

909 Venkatesan, R., Nagarajan, N.R., Paso, K., Yi, Y.B., Sastry, A.M., Fogler, H.S.,
910 (2005). The strength of paraffin gels formed under static and flow conditions.
911 Chemical Engineering Science 60(13), 3587-3598.

912 Walstra, P., Kloek, W., van Vliet, T., (2001). Fat crystals networks, in: Sato, K., Garti,
913 N. (Eds.), *Crystallization processes in fats and lipid systems*. Marcel Dekker, New
914 York, USA, pp. 289-328.

915

Manuscript submitted to ***Journal of Food Engineering***

A spinning disc study of fouling of cold heat transfer surfaces by gel formation from model food fat solutions

Huang, J.Y., Chew, Y.M.J. and Wilson, D.I.

Tables and Figures

Table 1. Experimental conditions employed in heat transfer experiments

	30 wt% Water/Glycerol	78 wt% Water/Glycerol	Paraffin[1]
Coolant temperature, T_{cw} (°C)	10.7	10.6	10.6
Bulk temperature, T_b (°C)	34.2 – 54.3	35.1 – 60.7	35.9 – 61.4
Dynamic viscosity, μ_b (Pa s)	0.0015 – 0.006	0.01 – 0.03	0.03 – 0.08
Reynolds number, Re_r	303 – 5443	47 – 307	11 – 48

[1]density at 25 °C, 870 kg/m^3, and viscosity 0.166 Pa s at 20 °C; BDH Chemicals, UK

Figure captions

Figure 1. (a) Schematic of the operation of the SDA, (b) construction of the fouling cell plate. Dimensions are in millimeters (not to scale)

Figure 2. Effect of composition and cooling rate on model solution T_m and T_c. Loci drawn through the T_m data show regression fit to ideal solution, Equation (2). Lines drawn through T_c data sets as a guide to the eye.

Figure 3. Evolution of viscosity of 5 wt% PPP solutions while cooling in the rheometer at 5 K min^{-1}. Constant shear stress, 2 Pa. Regions A-D separated by vertical dashed lines discussed in text.

Figure 4. Effect of ω_d on Nu^* for different test solutions. Symbols: solid – 30 wt% glycerol-water solutions grey – 78 wt% glycerol-water solutions, open – paraffin. T_b = 50 ºC; (triangles) – T_{cw} = 10.6 ºC, (squares) T_{cw} = 10.6 ºC, (diamonds) T_{cw} = 10.7 ºC, (circles) T_{cw} = 10.7 °C. Locus shows trend described by Equation (5) with a = 0.50 (Sparrow & Gregg, 1959)

Figure 5. Flow patterns and temperature profiles in the SDA for disc rotation speed of 5.4 rad s^{-1}, Re_r = 27. Black arrows are velocity vectors. Colour indicates temperature, dark red = 60 ºC (T_b), dark blue = 9.8 ºC (T_{cw}).

Figure 6. Effect of Re_r on the thermal resistances in the SDA: circle – $1/U$, triangle – $1/h_b$ from simulation, square – R_{cw} and line – R_w. Temperatures as in Figure 5.

Figure 7. (a) Temperature and (b) average shear stress on the disc surface at the radial location from 0 to 0.035 m, extracted from CFD simulations for various T_c and ω_d.

Figure 8. (a) R_f and (b) estimated T_s and T_w during fouling of 5 wt% PPP solutions at T_{cw} = 9.8 ºC, ω_d = 5.4 rad s^{-1}. Vertical dashed line in (*a*) separates linear rate stage from the falling rate stage. Horizontal dashed lines in (*b*) show salient temperatures for the 5 wt% solution used.

Figure 9. Initial transients for tests reported in Figure 8 and for solvent alone.

Figure 10. Correlation of R_f and m for fouling runs in Figures 8, 15 and 17.

Figure 11. Evolution of deposit composition for deposits in Figure 8.

Figure 12. Comparison of cumulative H_T, H_O (= H_X+H_S) and H_X for fouling runs in Figures 8.

Figure 13. Comparison of deposition rates estimated from R_f data and maximum rate of PPP mass transfer for 12 h fouling experiment in Figure 8.

Figure 14. Growth rate of δ_f in the falling rate stage for fouling runs in Figures 8 showing linear dependence on ΔT. Line shows fit to linear trend.

Figure 15. Effect of ω_d on fouling behaviour. Conditions: T_{cw} = 9.8 ºC, t = 12 h. $T^*$and t^* are

end temperature and time of linear rate stage respectively.

Figure 16. Effect of ω_d on m and deposit composition for the fouling runs for the fouling runs in Figure 15.

Figure 17. Effect of T_{cw} on (a) fouling behaviour and (b) T_s profile. Conditions: ω_d = 5.4 rad s^{-1} and t = 12 hr.

Figure 18. Effect of T_{cw} on deposit (a) mass and (b) composition, for the fouling runs for the fouling runs in Figure 17. Vertical lines in (a) indicate the T_c and T_m.

Figure 19. Effect of deposit solids volume fraction on rheological parameters measured at 20 ºC. Solid data sets are those reported for similar PPP solutions by Nigo *et al.* (2009). Loci indicate power law trend lines (Equation (21)) fitted to the data sets: $G' = 9\times10^{7}\psi^{3.7}$; $\tau_{EL} = 2.9\times10^{5}\psi^{4.8}$ and $\tau_C = 2.4\times10^{5}\psi^{2.8}$.

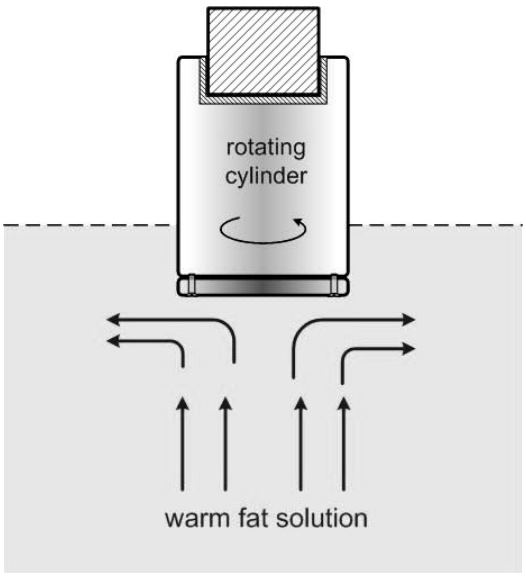

(a)

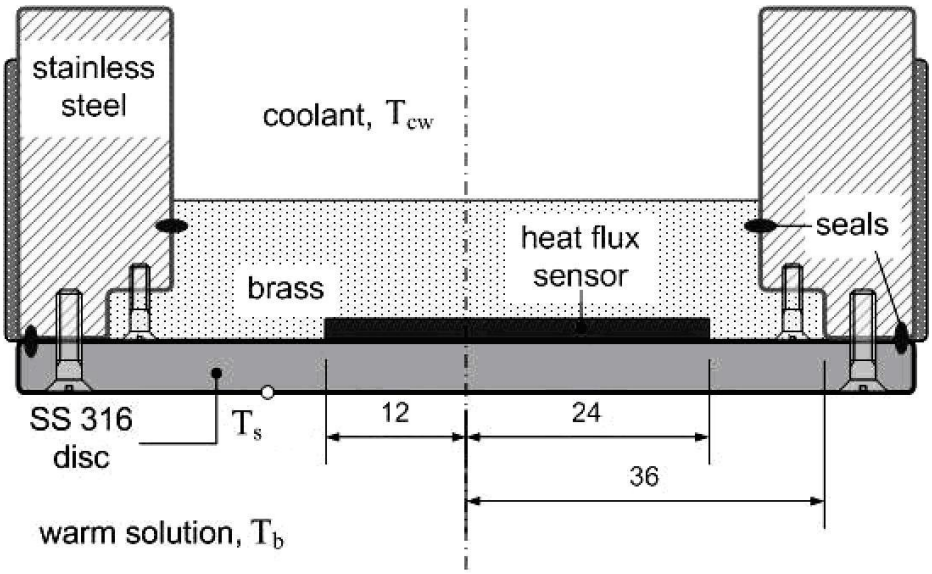

(b)

Figure 1. (a) Schematic of the operation of the SDA, (b) construction of the fouling cell plate. Dimensions are in millimeters (not to scale).

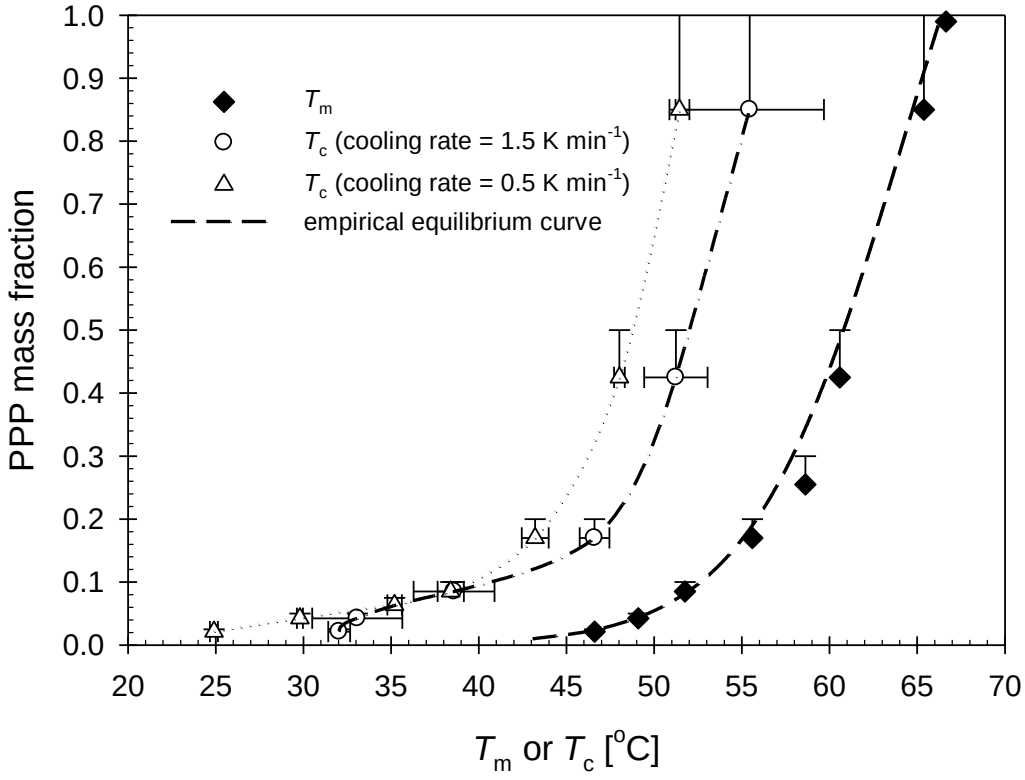

Figure 2. Effect of composition and cooling rate on model solution T_m and T_c. Loci drawn through the T_m data show regression fit to ideal solution, Equation (2). Lines drawn through T_c data sets as a guide to the eye.

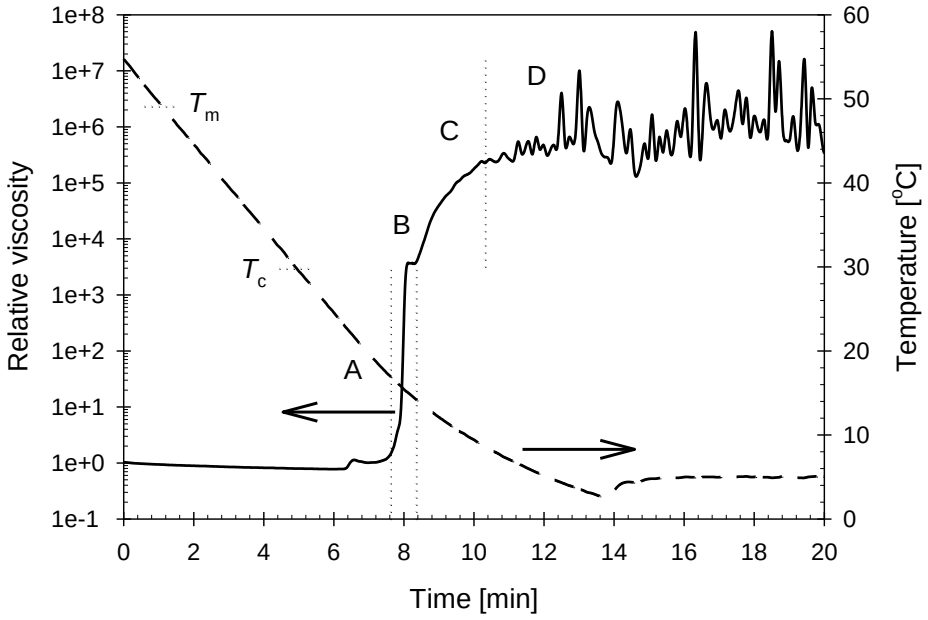

Figure 3. Evolution of viscosity of 5 wt% PPP solutions while cooling in the rheometer at 5 K min^{-1}. Constant shear stress, 2 Pa. Regions A-D separated by vertical dashed lines discussed in text.

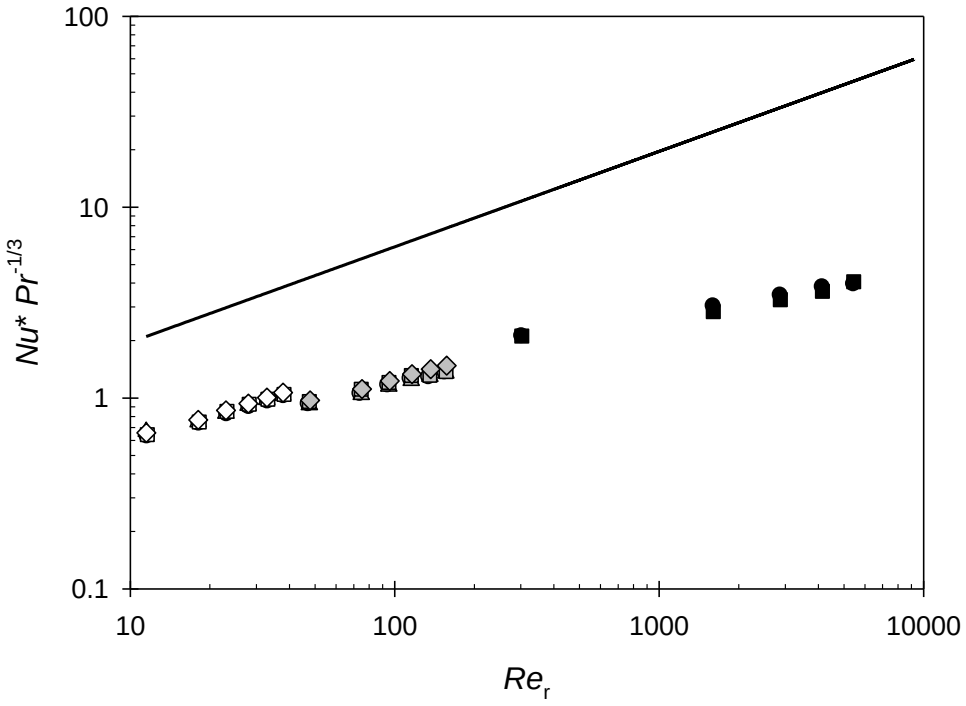

Figure 4. Effect of ω_d on Nu^* for different test solutions. Symbols: solid – 30 wt% glycerol-water solutions grey – 78 wt% glycerol-water solutions, open – paraffin. T_b = 50 ºC; (triangles) – T_{cw} = 10.6 ºC, (squares) T_{cw} = 10.6 ºC, (diamonds) T_{cw} = 10.7 ºC, (circles) T_{cw} = 10.7 °C. Locus shows trend described by Equation (5) with a = 0.50 (Sparrow & Gregg, 1959) .

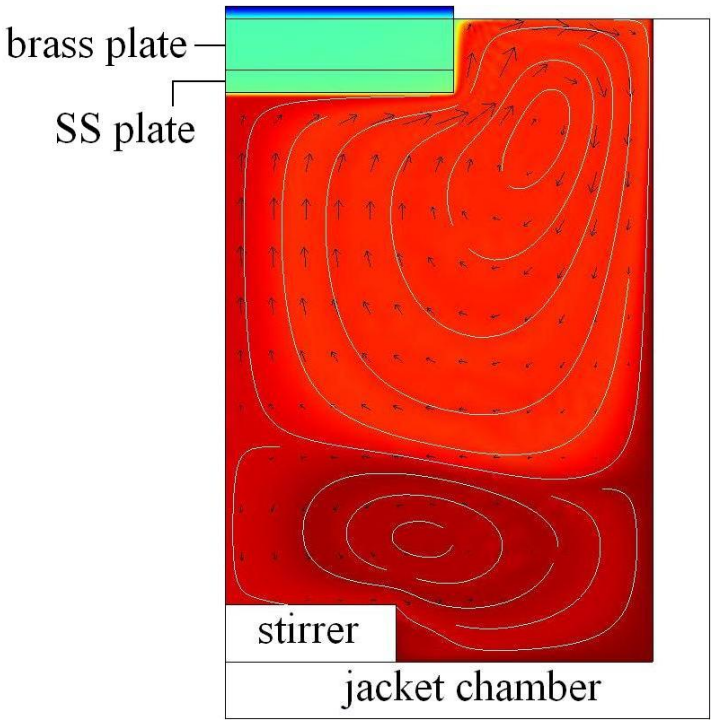

Figure 5. Flow patterns and temperature profiles in the SDA for disc rotation speed of 5.4 rad s^{-1}, Re_r = 27. Black arrows are velocity vectors. Colour indicates temperature, dark red = 60 ºC (T_b), dark blue = 9.8 ºC (T_{cw}).

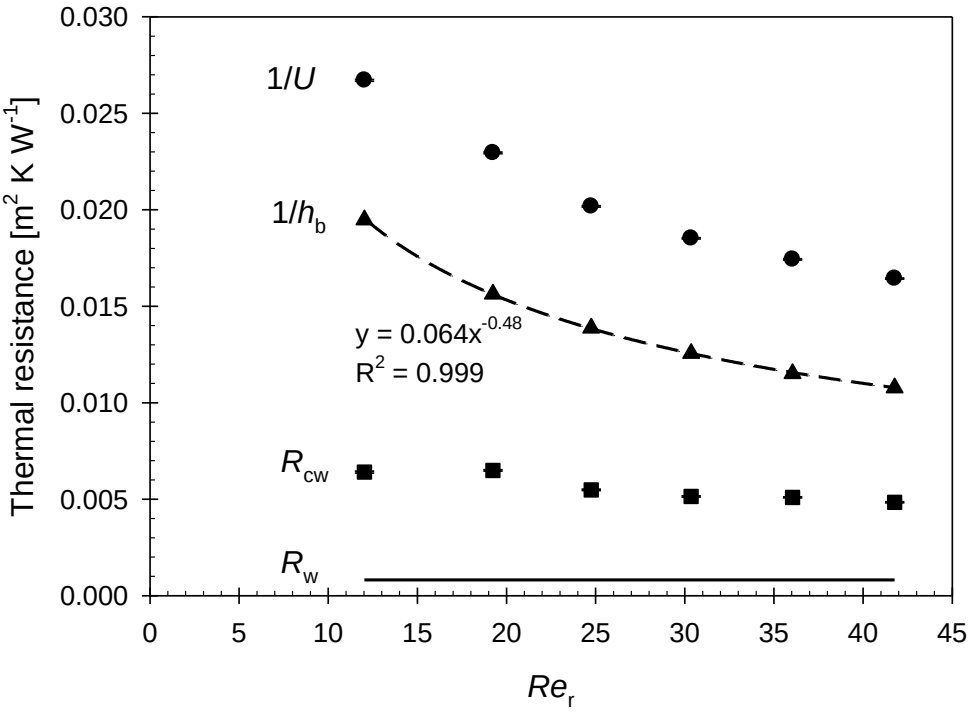

Figure 6. Effect of Re_r on the thermal resistances in the SDA: circle – $1/U$, triangle – $1/h_b$ from simulation, square – R_{cw} and line – R_w. Temperatures as in Figure 5.

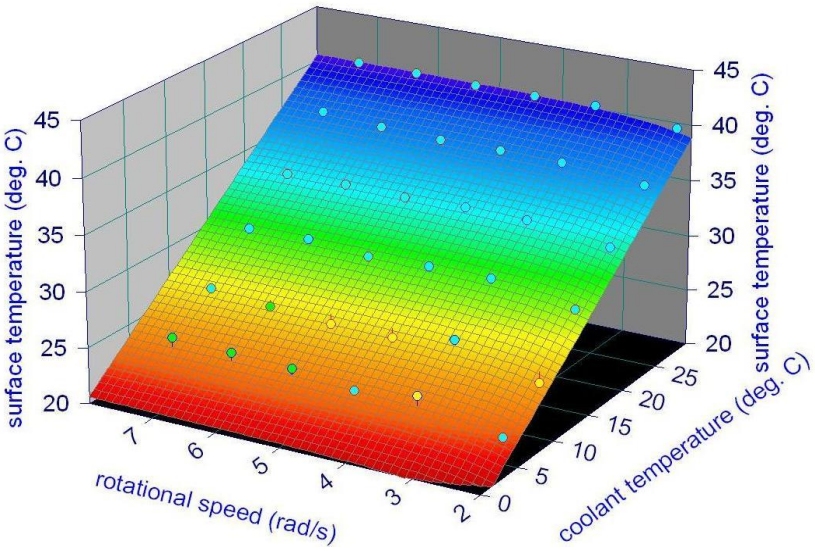

(a)

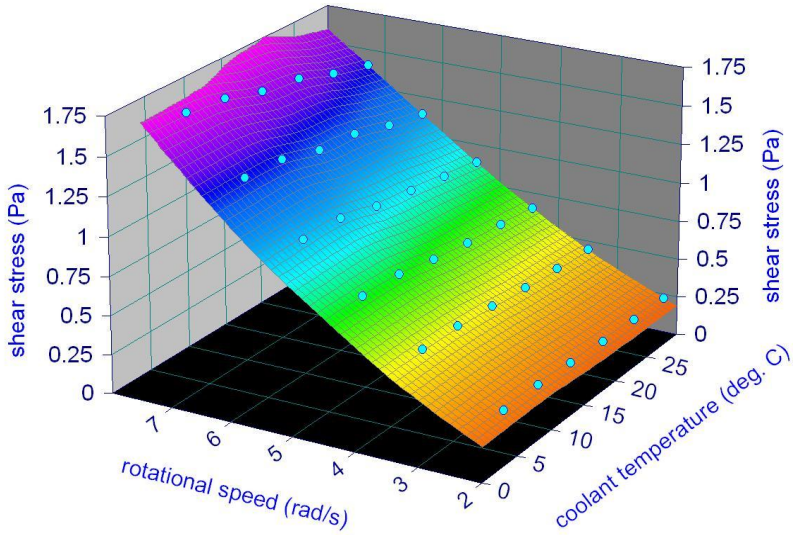

(b)

Figure 7. (a) Temperature and (b) average shear stress on the disc surface at the radial location from 0 to 0.035 m, extracted from CFD simulations for various T_{cw} and ω_d.

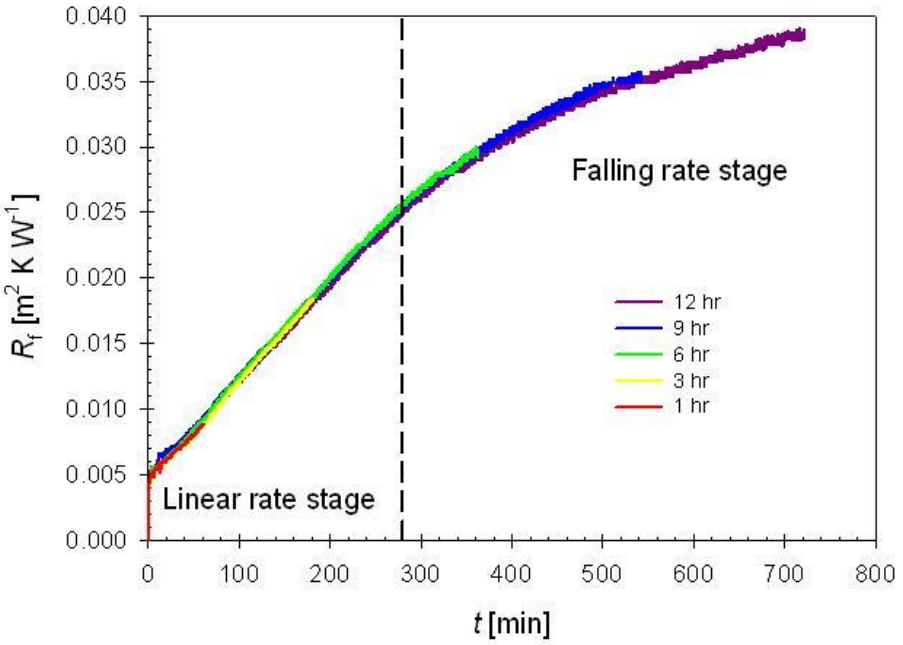

(a)

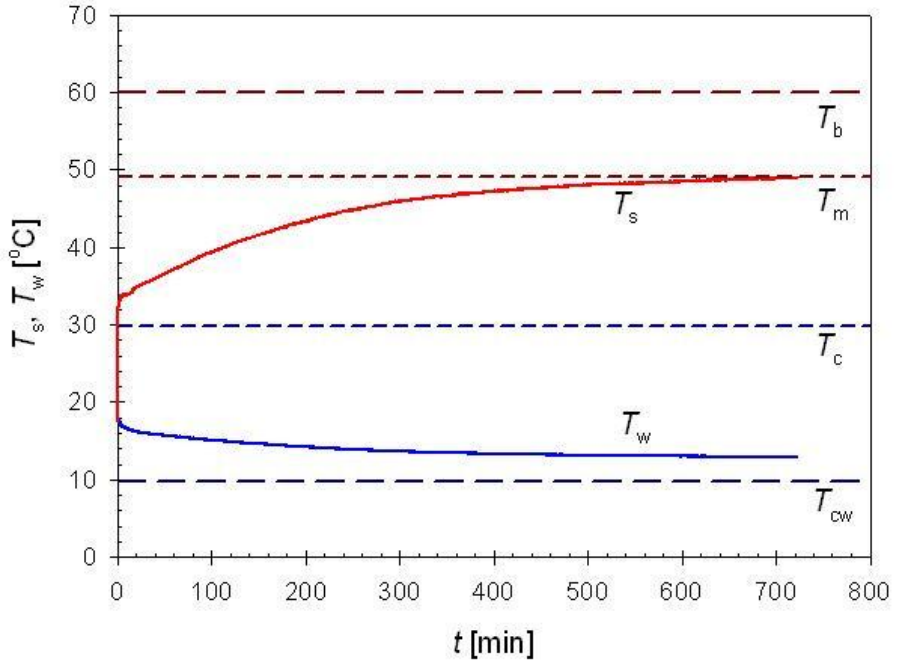

(b)

Figure 8. (a) R_f and (b) estimated T_s and T_w during fouling of 5 wt% PPP solutions at T_{cw} = 9.8 ºC, ω_d = 5.4 rad s^{-1}. Vertical dashed line in (*a*) separates linear rate stage from the falling rate stage. Horizontal dashed lines in (*b*) show salient temperatures for the 5 wt% solution used.

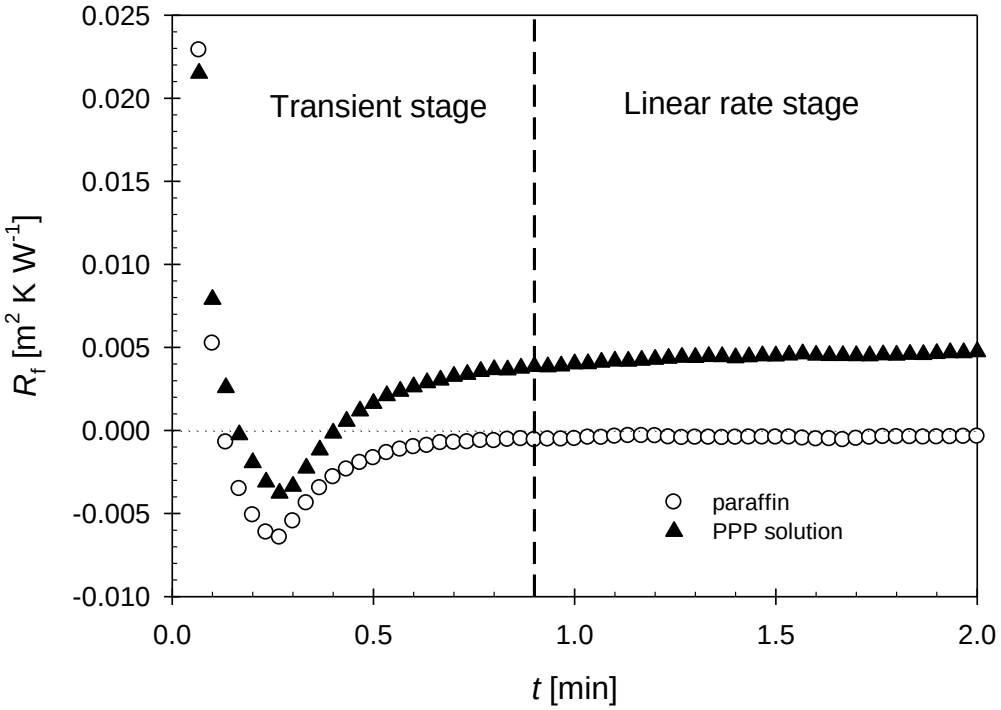

Figure 9. Initial transients for tests reported in Figure 8 and for solvent alone.

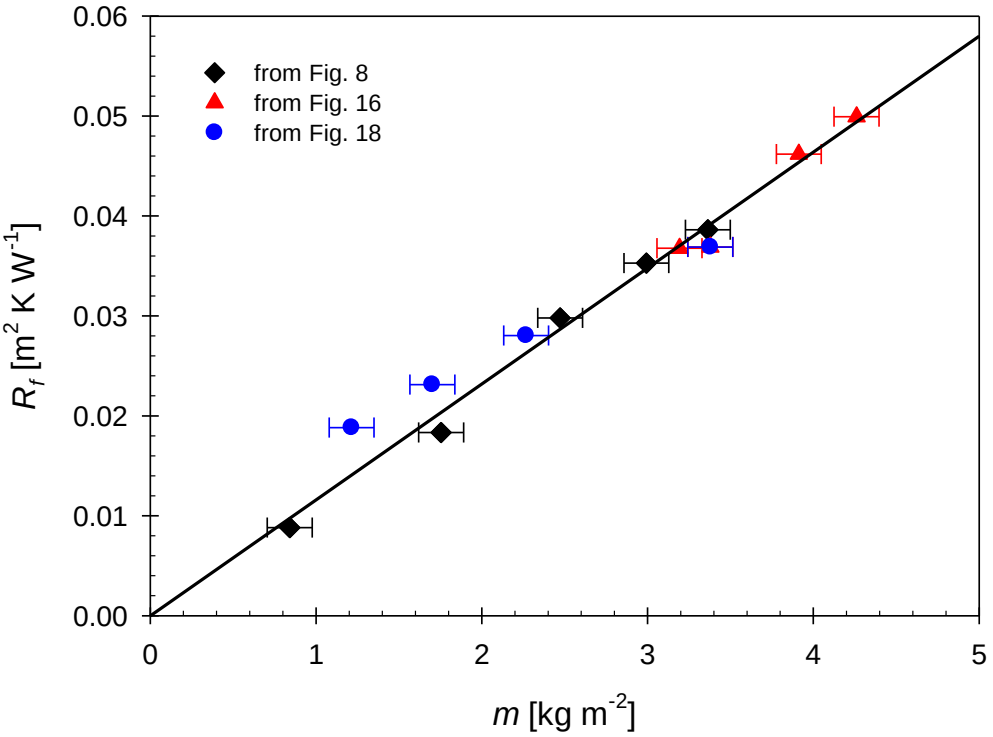

Figure 10. Correlation of R_f and m for fouling runs in Figures 8, 15 and 17.

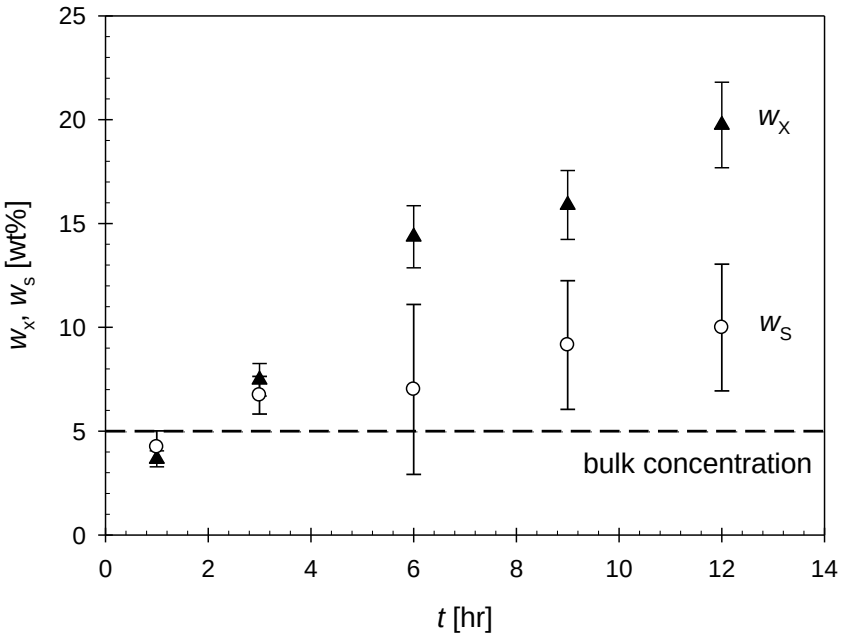

Figure 11. Evolution of deposit composition for deposits in Figure 8.

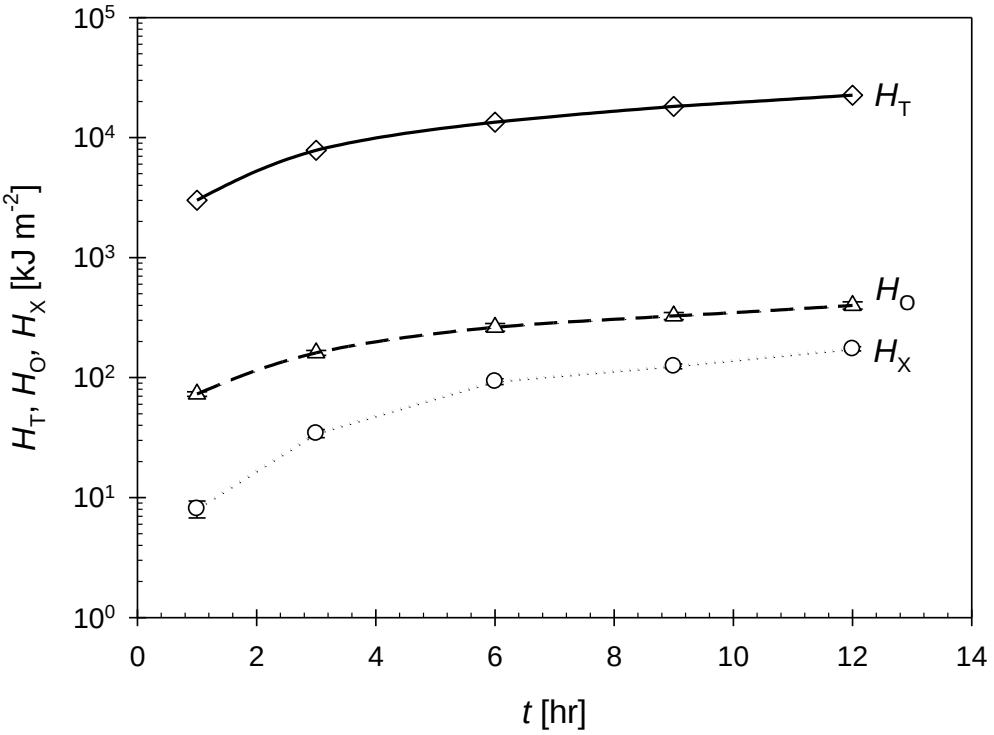

Figure 12. Comparison of cumulative H_T, H_O (= H_X+H_S) and H_X for fouling runs in Figures 8.

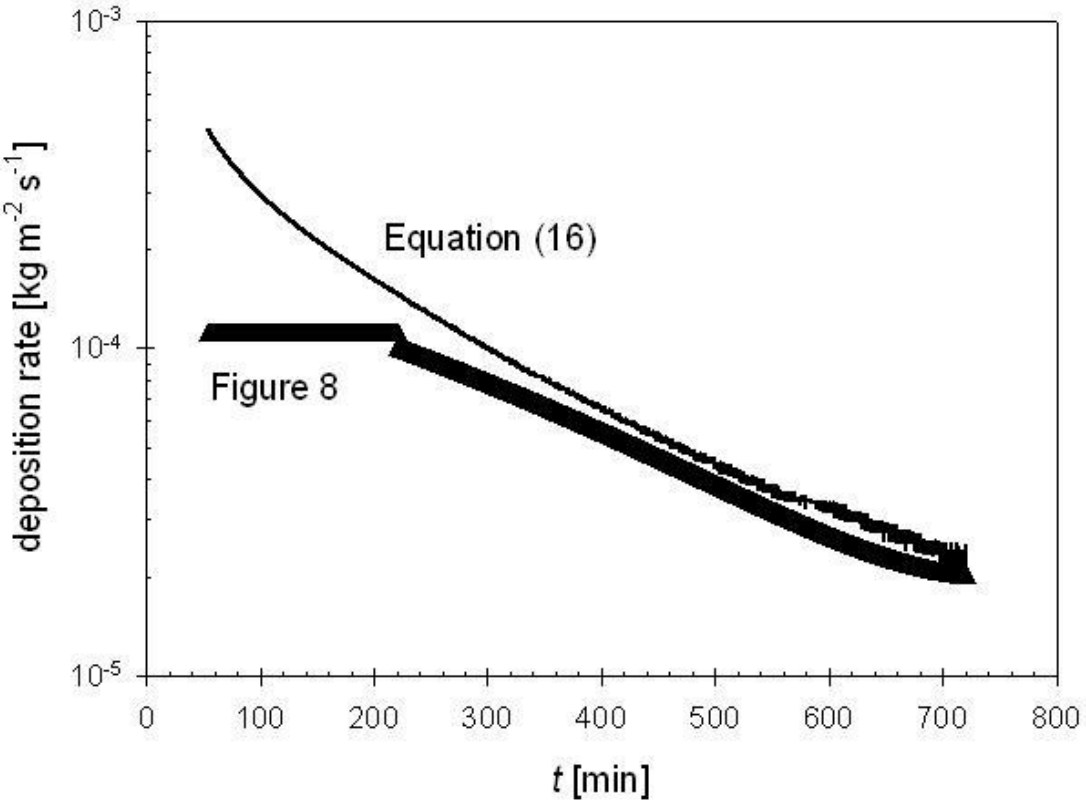

Figure 13. Comparison of deposition rates estimated from R_f data and maximum rate of PPP mass transfer for 12 h fouling experiment in Figure 8.

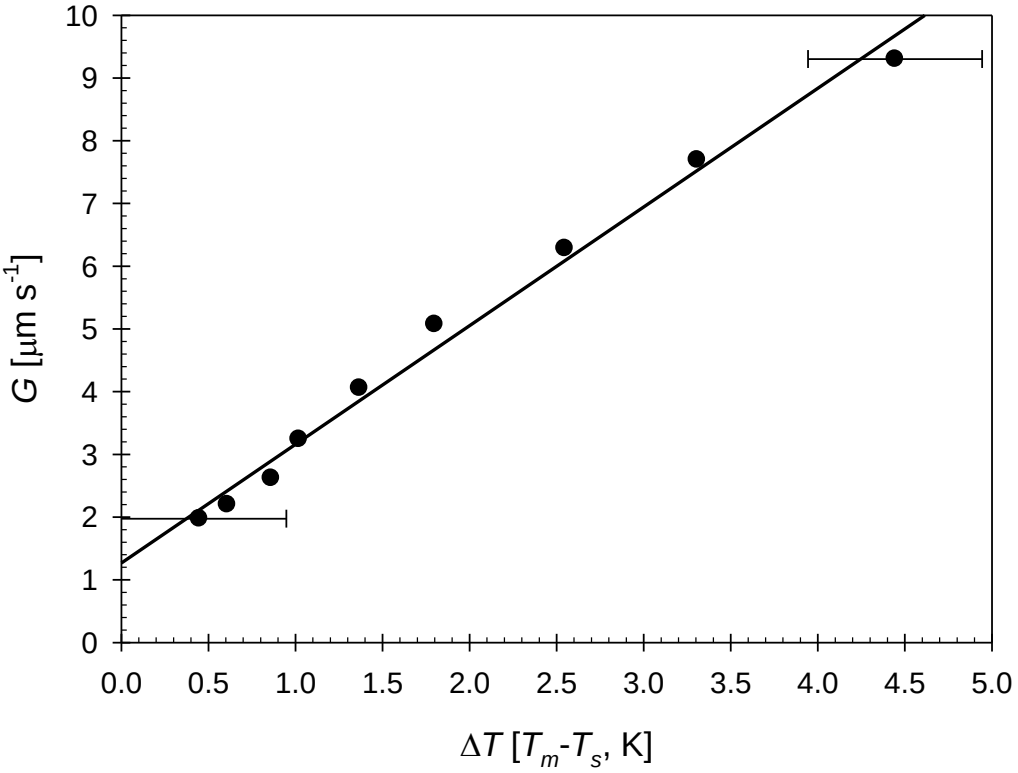

Figure 14. Growth rate of δ_f in the falling rate stage for fouling runs in Figures 8 showing linear dependence on ΔT. Line shows fit to linear trend.

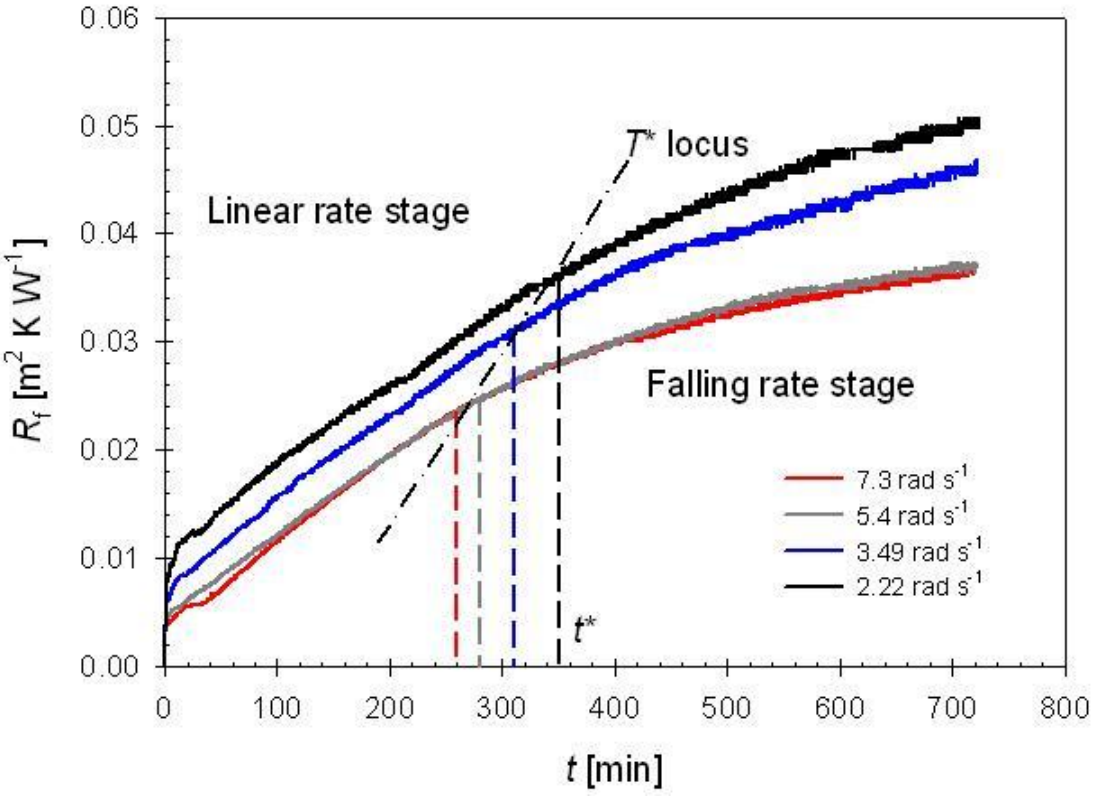

Figure 15. Effect of ω_d on fouling behaviour. Conditions: T_{cw} = 9.8 ºC, t = 12 h. T*and t* are end temperature and time of linear rate stage respectively.

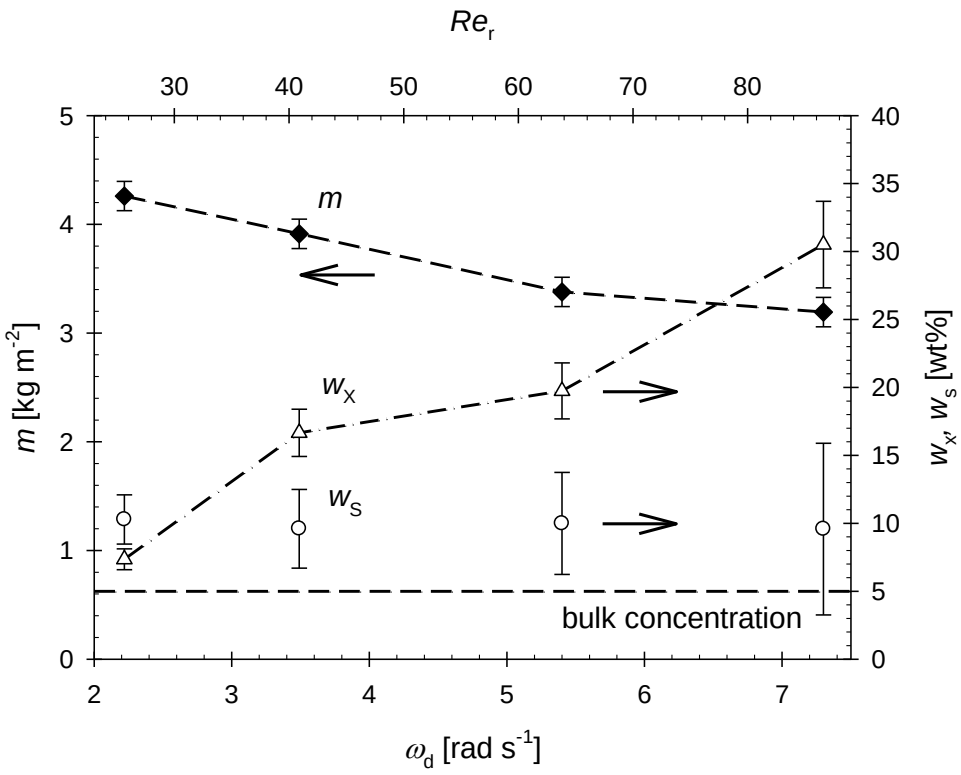

Figure 16. Effect of ω_d on m and deposit composition for the fouling runs for the fouling runs in Figure 15.

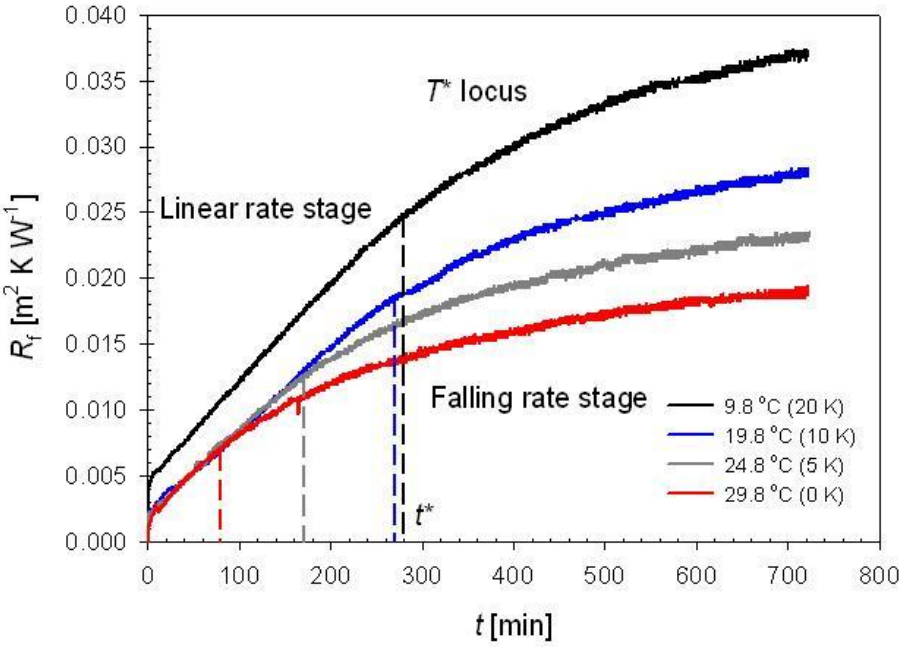

(a)

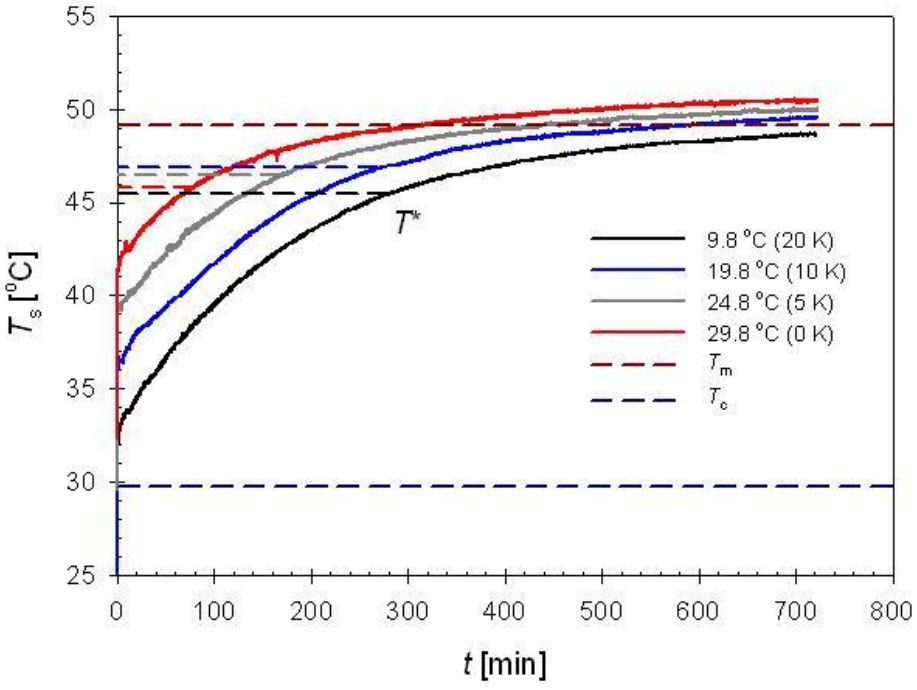

(b)

Figure 17. Effect of T_{cw} on (a) fouling behaviour and (b) T_s profile. Conditions: ω_d = 5.4 rad s^{-1} and t = 12 hr.

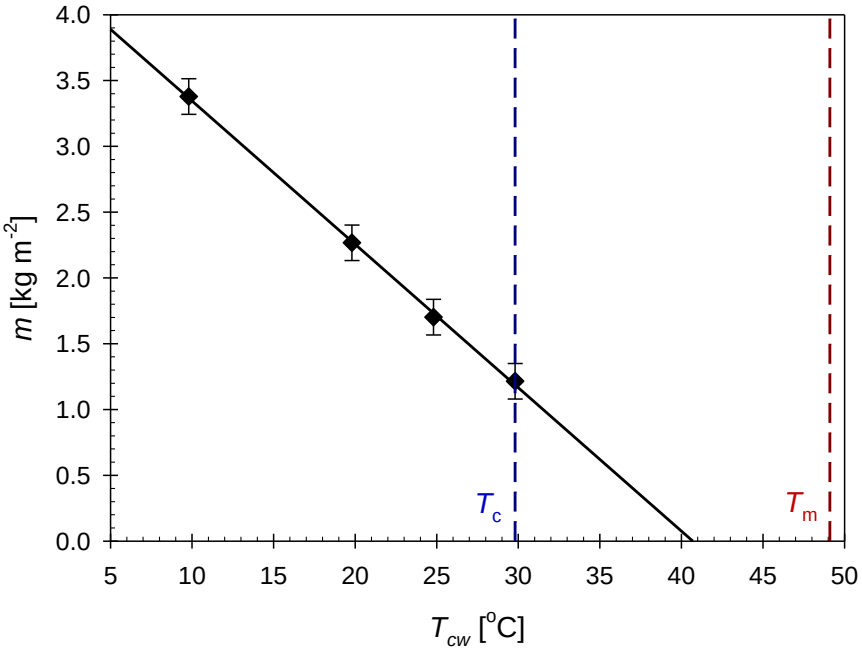

(a)

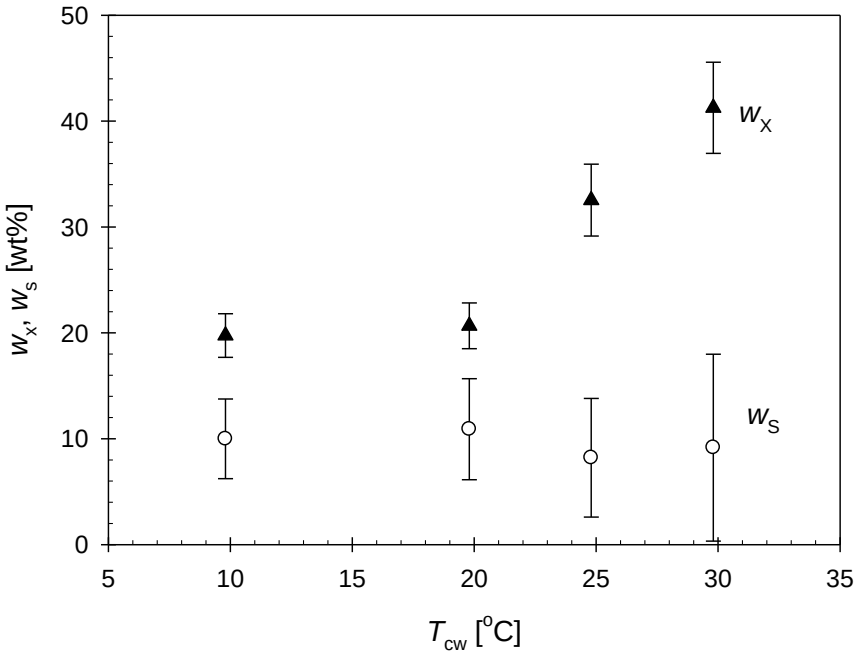

(b)

Figure 18. Effect of T_{cw} on deposit (a) mass and (b) composition, for the fouling runs for the fouling runs in Figure 17. Vertical lines in (a) indicate the T_c and T_m.

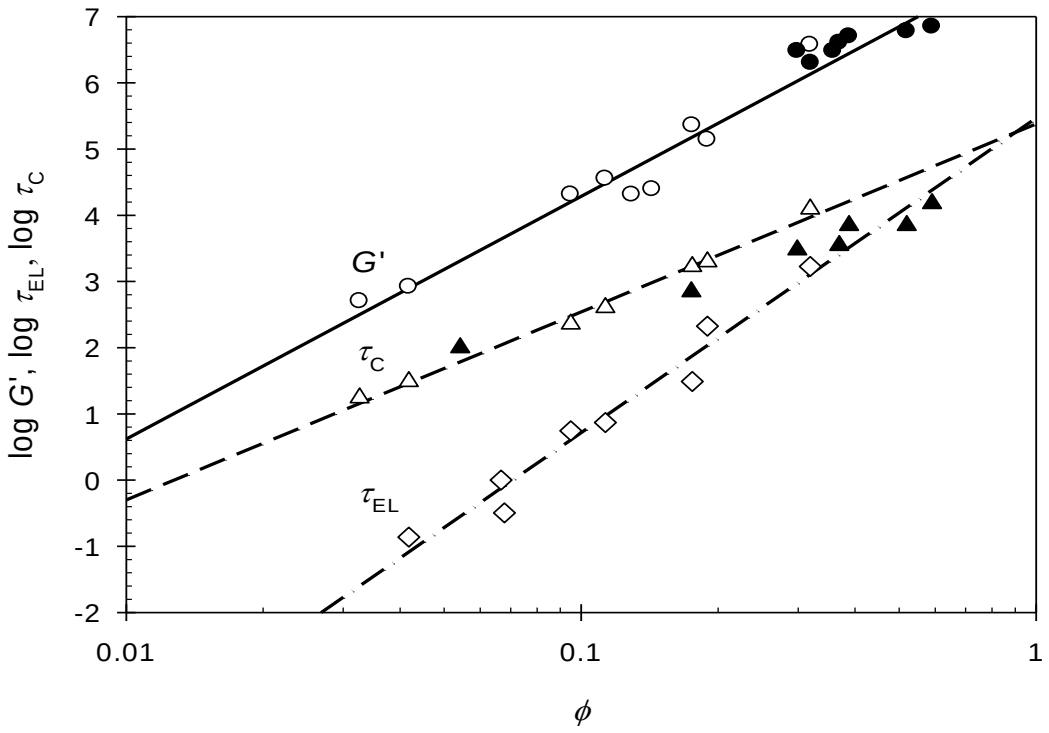

Figure 19. Effect of deposit solids volume fraction on rheological parameters measured at 20 ºC. Solid data sets are those reported for similar PPP solutions by Nigo *et al.* (2009). Loci indicate power law trend lines (Equation (21)) fitted to the data sets: $G' = 9\times10^{7}\psi^{3.7}$; $\tau_{EL} = 2.9\times10^{5}\psi^{4.8}$ and $\tau_C = 2.4\times10^{5}\psi^{2.8}$.